THE UNIVERSITY OF MICHIGAN

College of Engineering

Department of Mechanical Engineering

Cavitation and Multiphase Flow Laboratory

Report No. UMICH 01357-22-T

A PHOTOGRAPHIC STUDY OF SUBCOOLED FLOW BOILING AND THE BOILING CRISIS IN FREON-113

Ph. D. Thesis

by

Roger Joseph Mattson

Approved by: F. G. Hammitt

Financial Support Provided by:

National Science Foundation
Grant No. GK 1889

January 1972

ABSTRACT

A PHOTOGRAPHIC STUDY OF SUBCOOLED FLOW BOILING
AND THE BOILING CRISIS IN FREON-113

by

Roger Joseph Mattson

Chairman: Frederick G. Hammitt

This paper concerns an experimental investigation of the causal mechanisms in the subcooled flow boiling crisis. Freon-113 was used at moderate pressures of 100 to 350 psia to model water at high pressures of 800 to 2500 psia. This range includes the 2250 psia operating pressure of pressurized water nuclear reactors.

The research was motivated by the fact that there are no completely acceptable theoretical models of the departure from nucleate boiling (DNB) in subcooled flow boiling. To improve understanding of DNB and to facilitate the development of general theories to predict the critical heat flux it was necessary to disclose the detailed features of the two-phase flow regime and the changes, if any, in these features at the time of the boiling crisis. Photography was chosen as the experimental technique that could best accomplish that objective. Prior to this research there were no interpretable photographs of subcooled flow

boiling which had water pressures and mass flow rates above 1400 psia and 2 x 10^6 lb/hr-ft^2. For this photographic study the horizontal, rectangular flow channel with a narrow ribbon heater on the bottom surface was designed to minimize optical distortions and to provide an unobstructed view of the two-phase flow patterns.

The results of this research were high resolution, high speed, still and motion pictures of subcooled flow boiling before, during, and after DNB for a range of pressures, subcoolings, and mass flow rates. The following measurements were made from the photographs: bubble size, bubble size distribution, bubble population density, vapor velocity distribution, bubble boundary layer thickness, and the post-DNB vapor layer thickness. The average size of the largest bubbles and the thickness of the bubble boundary layer were correlated by a multiple linear regression analysis with the dimensional parameters of the experiment and with the controlling nondimensional parameters. These correlations generally agreed with those obtained by other investigators working at lower pressures and heat fluxes. In addition, the 39 critical heat flux data points obtained in the course of the research were successfully correlated by the equation of Dean for Freon-113.

The following conclusions were reached for the parameter ranges investigated.

The two-phase flow regime in high pressure subcooled boiling is bubbly in which small vapor bubbles form a flowing boundary layer along the heated surface. At high heat flux the thickness of the bubble boundary layer is much larger than the diameters of the largest bubbles.

Bubbles move along the heated surface at velocities which increase with size. The bubble size and size distribution on the heater increase as heat flux is increased and decrease as mass velocity is increased.

Bubbles coalesce on and above the heater. The largest bubbles occur at locations away from the heater and are the result of coalescence after departure from the heater.

The mechanism by which the wall void fraction increases with heat flux is first by simultaneous increases in bubble size and population density at low heat flux and then by increase in size and decrease in population density because of coalescence at high heat flux.

At DNB the local slip ratio between vapor and liquid velocities is greater than 1 except in a very thin region on the heated surface. The volume average slip ratio is apparently greater than 1 at DNB.

At DNB there are no abrupt changes in bubble size, bubble population density, bubble flow trajectory, bubble boundary layer thickness, or bubble boundary layer slope. That is, there is no abrupt change in flow regime at DNB.

A thin intermittent vapor layer forms on the heated surface at DNB. The thickness of the layer is approximately equal to the bubble departure size. It is thinner, however, than the diameters of the largest bubbles in the bubble boundary layer, and it is thinner than the bubble boundary layer by approximately a factor of ten.

A PHOTOGRAPHIC STUDY OF SUBCOOLED FLOW BOILING AND THE BOILING CRISIS IN FREON-113

by
Roger Joseph Mattson

A dissertation submitted in partial fulfillment
of the requirements for the degree of
Doctor of Philosophy
(Mechanical Engineering)
in The University of Michigan
1972

Doctoral Committee:

Professor Frederick G. Hammitt, Chairman
Assistant Professor Louis J. Hamilton
Associate Professor Edward R. Lady
Professor Herman Merte, Jr.

To Judith

who shared the "going-ups and the coming-downs,
walking pneumonia and run-of-the-mill madness,
colored with guilt, pride, and
a vague sense of despair--"[38]

ACKNOWLEDGMENTS

I thank the following people and institutions --the former for their humanity, the latter for their money:

Professor Fred Hammitt who listened,
Dr. Long Sun Tong who talked about science,
Dr. Morris Rosen who arranged the transportation,
Ed Rupke who cared about what he built,
Ed Timm who knew where everything was,
Paul Fessler who quietly measured bubbles,
Mother Waser who was always there,
The United States Atomic Energy Commission, The National Science Foundation, and The Department of Mechanical Engineering of The University of Michigan who provided fellowships, and
The Michigan Memorial Phoenix Project, The National Science Foundation, and The Department of Mechanical Engineering of The University of Michigan who provided financial support for the research.

CONTENTS

TABLES

FIGURES

NOMENCLATURE

b	Width of heated surface, inch
Bo	Boiling number = $q''/h_{fg}G$
C_p	Specific heat at constant pressure, Btu/lbm-F
D	Diameter, inch
D_b	Average diameter of largest bubbles, inch
D_e	Equivalent diameter, inch
Fr	Froude number = V^2/gD
g	Gravitational acceleration, ft/sec^2
g_c	Conversion factor, $ft\text{-}lbm/lbf\text{-}sec^2$
G	Mass flow rate, $lbm/hr\text{-}ft^2$
h	Enthalpy, Btu/lbm
Δh	Enthalpy subcooling = $h_{local} - h_{sat}$, Btu/lbm
h_{fg}	Latent heat of evaporation, Btu/lbm
L	Length, inch
p	Pressure, psia
p.d.	Bubble population density, $inch^{-3}$
p_r	Reduced pressure = p/p_{crit}
Pr	Prandtl Number = $\mu C_p/k$
Q	Volumetric flow rate, ft^3/hr
q"	Heat flux, $Btu/hr\text{-}ft^2$
Re	Reynolds number = $\rho VD/\mu$
s	Local slip ratio
$\bar{s}$	Volume average slip ratio

St	Stanton number = $q''/C_p \Delta T_{sc} G$
t	Time, second
T	Temperature, F
ΔT_{sc}	Temperature subcooling = $T_{sat} - T_b$, F
v	Specific volume, ft^3/lbm
V	Velocity, ft/sec
X	Quality, ratio vapor mass velocity to total mass velocity
y	Vertical distance from channel wall, inch
y_o	Half-height of channel, inch
α	Void fraction, ratio vapor area to total area at a channel cross section
δ	Bubble boundary layer thickness, inch
μ	Viscosity, lbm/ft-hr
ρ	Density, lbm/ft^3
σ	Surface tension, lbf/inch

Subscripts

b	Bulk or main stream condition
crit	Critical condition
cl	Channel centerline
i	Inlet condition
l	Liquid
sat	Saturation condition
sc	Subcooling
v	Vapor

Chapter 1

INTRODUCTION

Background

Nucleate boiling is an efficient means for transferring large quantities of heat within relatively small volumes. There is a limit on the maximum heat transfer rate and it is described by the term "boiling crisis." It occurs because of the transition from high efficiency nucleate boiling to low efficiency film boiling; i.e., from discrete vapor bubbles to a continuous vapor film on the heated surface. The transition is characterized by a sharp increase in surface temperature caused by greatly increased thermal resistance of the fluid adjacent to the heated surface. This transition point is also called "burnout" or "departure from nucleate boiling (DNB)." The maximum nucleate boiling heat flux is called "critical heat flux (CHF)."

The mechanisms of the flow boiling crisis are known to be closely related to flow patterns. Diabatic two-phase flow patterns can be roughly classified into two categories, as shown in Figure 1. In subcooled flow boiling with high heat flux and high flow rate the bubbles are small and more concentrated near the heated surface. The two-phase fluid in the wall region is not in thermodynamic equilibrium

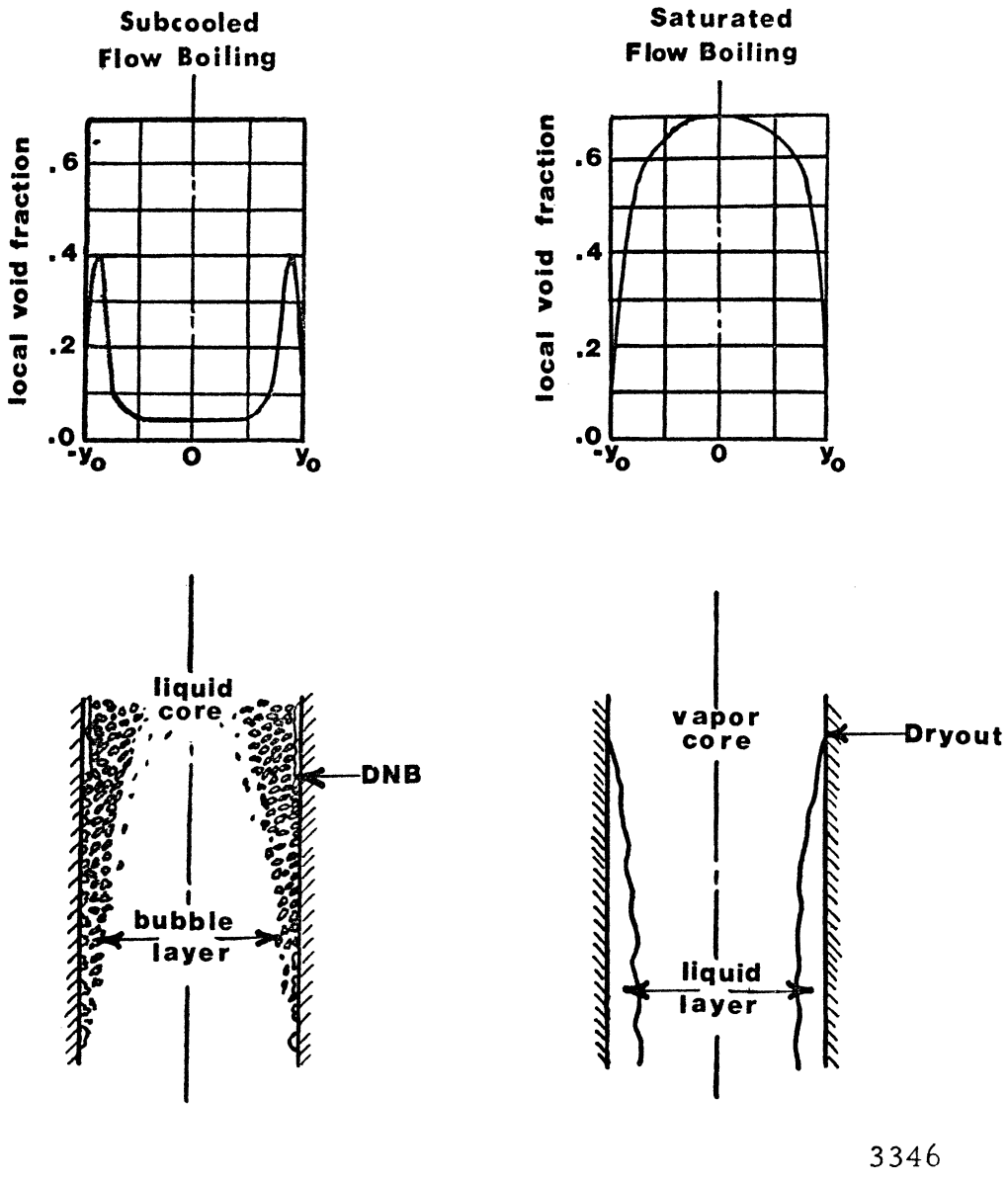

Figure 1. Two categories of diabatic two-phase flow, after Tong[1].

with the subcooled bulk stream. This produces a peak in the local void fraction which impairs cooling by reducing communication between the subcooled liquid and the heated surface. When DNB occurs a vapor layer insulates the surface and the high heat flux causes the surface temperature to rise rapidly to a high value (fast burnout).

In saturated flow boiling with high heat flux and high flow rate a liquid layer flows adjacent to the heated surface and a vapor core flows outside the liquid layer. When the liquid film becomes sufficiently thin a dry patch forms at the heated surface (dryout). Boiling crisis occurs when the surface temperature exceeds the Leidenfrost temperature. After DNB the fast moving vapor core continues to provide relatively good heat transfer, so the surface temperature transient is slow and surface melting may not occur (slow burnout).

Theoretical efforts to predict CHF have been more successful in the saturated category of flow boiling primarily because it has been easier to observe hydrodynamic mechanisms which cause the film dryout under these conditions. For example, high-speed motion photography by Tippets[2] provided the physical bases for theoretical prediction of CHF in saturated boiling of water at high pressure.

On the other hand, there is no completely acceptable theoretical model of the forced convection, subcooled boiling crisis. It is more difficult to observe the very small, concentrated bubbles typical of this flow boiling regime, and prior to this research there were no interpretable pictures of the bubbly flow regime for pressures above about 1400 psi and flow rates above about 2×10^6 lbm/hr-ft^2 in water. Previous work on subcooled burnout has emphasized empirical correlations of CHF data, however, there are a few theoretical models and these are summarized below.

Bankoff[3] developed a two-region model in which heat was first transferred from the wall to a two-phase layer of fluid and then into a subcooled core of liquid. He postulated that bubble population and size increase as DNB is approached indicating a buildup in energy content of the two-phase region. He said that the boiling crisis occurs because the turbulent core is unable to remove heat from the two-phase layer as fast as heat is transmitted from the wall. This model failed to predict CHF because of its inability to quantitatively describe heat transfer in the two-phase layer.

Chang[4] formulated two DNB models based on the dynamics of (1) large individual bubbles with no viscous effects for

low velocity boiling, or (2) small bubbles concentrated in a viscous boundary layer for high velocity boiling. In the latter case, the bubble boundary layer was analytically found to approach a critical velocity independent of further increases in main stream velocity. This reinforced the theory that burnout is associated with the increasingly effective isolation of the heated surface from the subcooled main stream by the two-phase boundary layer.

Weatherhead[5] found that when critical heat flux occurs in low quality flow boiling it is directly dependent upon the degree of hydrodynamic instability. The hydrodynamic instability was thermally induced in his experiments by lowering the inlet subcooling to a boiling channel of otherwise constant parameters. He observed that the bubbles coalesced; this resulted in slug flow followed by hydrodynamic instability and then DNB.

Gambill[6] proposed that CHF in subcooled flow boiling could be predicted by summing a critical pool boiling term and a critical forced convection term. This technique is open to question because fluid and bubble dynamics of flow boiling are different from those of pool boiling.

Tong, et al.[7] suggested a DNB model based on a three-region flow pattern: a superheated liquid layer on the heated wall, a bubble layer, and a subcooled core of liquid.

They said that the energy content of the superheated layer is representative of wall heat flux and wall temperature, and thus it identifies the local thermal conditions at DNB. This was expressed by a limiting enthalpy of the superheated layer which was empirically evaluated from CHF data.

Tong[8] extended Kutateladze's[9] analogy between subcooled boiling in turbulent flow and gas injection into a turbulent boundary layer. The visualized model is a bubble boundary layer on the heated surface, and the transverse momentum of vapor generation is conceptualized as mass injection into the boundary layer. When the transverse momentum reaches a critical fraction of the free stream momentum the boundary layer stagnates and then separates from the wall. The stagnant fluid completely evaporates and forms a vapor blanket because of high surface heat flux. The local wall temperature rises and the boiling crisis is complete when the Leidenfrost temperature is exceeded. Using this model Tong obtained a reasonably good correlation of water and Orthoterphenyl CHF data, but the equation he used had several empirical constants.

Dean[10] experimentally verified that bubble boundary layer instability (separation) could be initiated either by subcooled vapor injection through a porous wall or by subcooled boiling on the wall. Similar equations were

used to predict critical conditions for boiling, for injection, and for a combination of the two.

Wallis[11] suggested a DNB analysis based on the Reynolds flux concept. He visualized a mass flux at the heated surface to account for momentum and vapor flux normal to the main stream flow. According to this model the boiling crisis occurs when the transverse flux of vapor equals the transverse momentum flux; i.e., the net mixing flux at the wall is zero. Tong[12] has shown that this condition is equivalent to zero wall friction at DNB, and thus it coincides with the boundary layer separation condition.

Fiori and Bergles[13] used photographic and electric probe studies to show that in low pressure, subcooled boiling the formation of slug flow precedes DNB. They suggested a boiling crisis model based on the formation of a dry spot beneath a vapor slug.

Motivation

The primary criticism of subcooled DNB theories is that they are based on presumed flow structures and assumed sequences of hydrodynamic events. Furthermore, none of the theories predict CHF as accurately as empirical correlations of CHF data. Empirical correlations, unfortunately, have been derived for specific systems and are not generally applicable to other systems.

To improve understanding of DNB and to develop general theories to predict CHF, it is necessary to observe the real physical events. Information is needed which discloses detailed thermal-hydraulic features of the two-phase flow regime at DNB. Such data are available for some conditions, namely: saturated boiling[2], and low pressure subcooled boiling.[13,14] The DNB mechanism in high pressure, high velocity subcooled flow boiling has not previously been studied in a detailed mechanistic manner. These boiling conditions are important because they include the operating conditions of pressurized water nuclear reactors.

Photography has been used to study many facets of two-phase flow, e.g., cavitation bubble collapse, boiling inception, bubble growth, flow regimes, point of net vapor generation, boiling crisis in pool boiling and in annular flow, and injection cooling. In most cases where photography was used as the primary experimental technique (as opposed to many experiments observed by photography but not dependent upon photographs as the primary data source) valuable insights were gained concerning the controlling physical mechanisms.[15]

Photography has not been used before for detailed study of the mechanisms controlling the high pressure, subcooled boiling crisis. Several obstacles have prevented such studies: (1) the small size of bubbles--from 0.001 to 0.010 inch, (2) the high mass velocity of interest for

application to reactor technology--about 2 x 10^6 lb/hr-ft^2, and (3) the high pressure of interest for application to reactor technology--about 2000 psi in water. Small bubbles and high velocity demand high resolution, high speed photography while high pressure complicates design and construction of high resolution, transparent test sections. These obstacles were overcome in this research by careful application of high speed still and motion photography and by use of another fluid at low pressure to model water at high pressure.

In recent years, many researchers have modeled two-phase hydrodynamic phenomena with Freon* refrigerants to facilitate experiments not economically or technically feasible at the power, temperature, or pressure demanded by the prototype fluid. Freon-113 was selected as the modeling fluid for this research because (1) system pressure is reduced by a factor of approximately six for flow patterns and bubble sizes equivalent to those in water[16,17], (2) heating power is reduced by a factor of approximately 10 compared to water[17,18], and (3) there has been much recent work using Freon in two-phase flow scaling.[16-23] A summary of recent works concerning the modeling of two-phase phenomena is given in Appendix A.

---

*DuPont trademark

Objective

The objective of this research was to observe the bubble boundary layer at the location of the boiling crisis in high pressure, subcooled flow boiling with high resolution, high speed still and motion photography. The observations included measurements from photographs of the bubbles and the bubble boundary layer and photographic records of the flow structure before, during, and after DNB for several flow rates, subcoolings, and pressures. The parameter ranges generally covered the operating conditions of pressurized water reactors. The dominant flow mechanisms at DNB were judged for the conditions tested on the basis of the photographic information. Critical heat flux data for Freon-113 were recorded and correlated by the equation of Dean[10].

Chapter 2

THE FACILITY

Loop

This research required the design and construction of a new boiling heat transfer facility in the Mechanical Engineering Department's Cavitation and Multiphase Flow Laboratory at The University of Michigan. Most of the components in the new facility were salvaged from a loop used for cavitation studies in mercury. All such components were thoroughly cleaned before installation in the new loop.

The Freon facility is shown schematically in Figure 2. Individual components are described in Appendix B. All components in contact with Freon were constructed of 300-series stainless steels. Design pressure was 400 psig at 350°F for all components except the storage tank. The loop was pressure tested to 350 psig at 270°F, the most extreme test conditions of this research. It is unsafe to over-pressure test glass components such as the transparent test section which cannot be missile shielded during normal operation.[10] Flow through the loop was limited to a minimum of 3 gpm because of intense pump vibration when operating

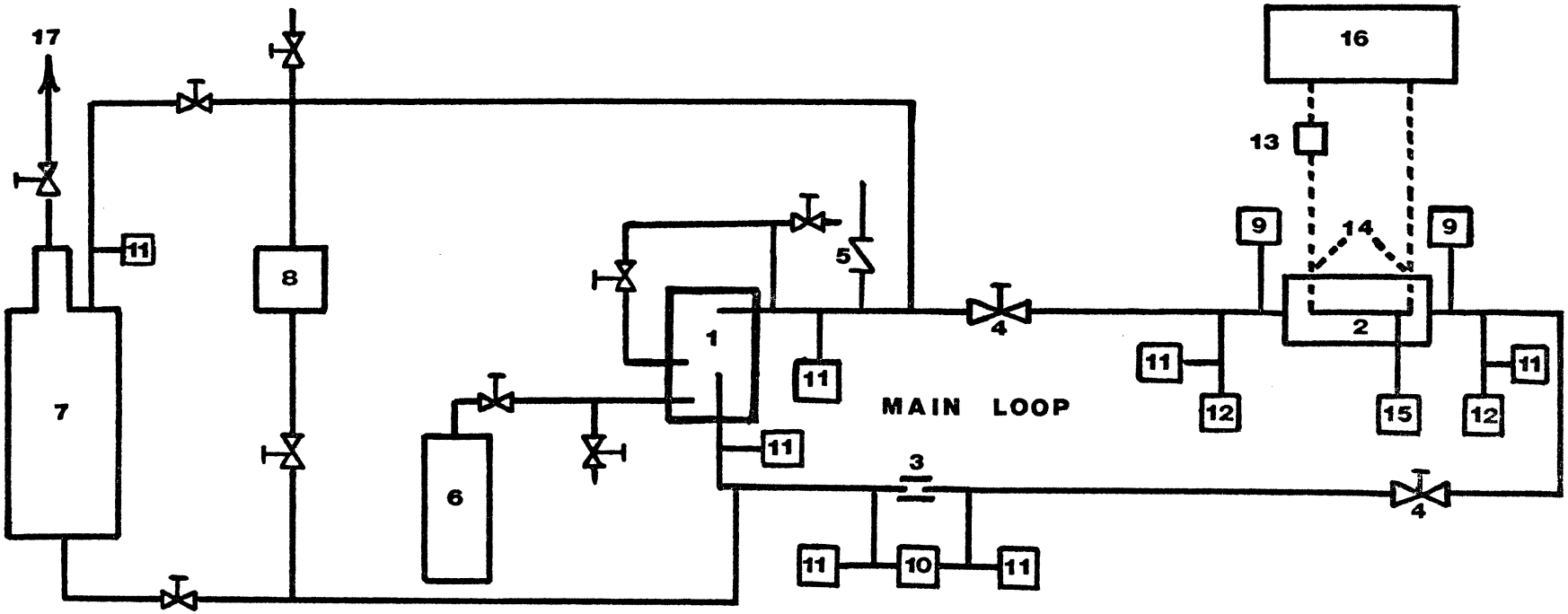

1. Centrifugal pump
2. Test section
3. Flow orifice
4. Throttle valves
5. 400 psi relief valve
6. Compressed dry air
7. Storage tank
8. Filter-dryer
9. Coolant thermocouples
10. Transaire Δp transmitter
11. Heise pressure gage manifold
12. Taylor pressure gages
13. Current shunt
14. Voltage tap
15. Heater thermocouple
16. Power supply
17. Air compressor

3347

Figure 2. Schematic diagram of the loop.

near its shutoff head. The maximum coolant temperature was limited to 270°F because heat loss matched heat input from the a.c. clam shell heaters at this coolant temperature.

Coolant

Freon-113 is a colorless liquid with a typical cleaning solvent odor. At atmospheric pressure its boiling point is 117.6°F. At room temperature its vapor pressure is 5.5 psia; this results in rapid evaporation upon spilling or leaking. The properties of liquid Freon-113 are given in Table 1.

Freon-113 has several peculiarities which must be considered in designing heat transfer equipment. Two examples are (1) its low surface tension, which causes equipment sealing difficulties; and (2) its high air solubility, which is of concern in nucleation or boiling initiation studies. These and other nuances of working with Freon-113 are thoroughly described in Reference 26. The high air solubility of Freon-113 is not a problem in DNB studies. This conclusion is based on the work by Murphy and Bergles[26] who found that dissolved air affects boiling Freon-113 only in the regions of incipient and developing flow boiling. In their study air content variations did not affect fully

T °F	P_{sat} psia	ρ_l lb/ft^3	ρ_v lb/ft^3	h_l Btu	h_{fg} Btu/lb	C_p Btu/lb-F	μ_l lb/hr-ft	σ 10^{-4} lb/in	Pr -----
70	5.52	98.26	0.185	22.48	66.56	0.223	1.66	1.18	8.5
100	10.5	95.79	0.336	28.99	64.46	0.229	1.36	1.99	7.5
150	25.9	91.44	0.786	40.38	60.44	0.239	1.02	0.80*	6.4
200	54.7	86.76	1.602	52.45	55.62	0.249*	0.78	0.62	5.7*
250	101.8	81.71	2.953	62.87	51.01	0.259	0.62*	0.44	5.2
300	175.6	75.63	5.272	75.82	44.33	0.269	0.51	0.26	5.0
350	283.3	67.80	9.489	90.12	34.68	0.279	0.42	0.10	4.93
400	434.3	55.02	20.54	105.78	16.84	-----	----	----	----
417.4	498.9	35.96	35.96	109.49	0	-----	----	----	----

Table 1. Thermal and transport properties of Freon-113.

(*Indicates that property values were extrapolated above this temperature.)

developed flow boiling heat transfer rates and no consistent effect on critical heat flux was found for variations in dissolved air. In the present study the Freon-113 was partially deaerated during loop heatup when loop pressure was periodically relieved through a shut-off valve to the storage tank. Loop operating pressure was achieved by admitting compressed dry air to the far end of a ten-foot length of 1/4-inch diameter tubing which connected to the pump sump.

The word "Freon" is DuPont's registered trademark for selected halogenated compounds containing fluorine. These compounds are used commercially and industrially with few safety restrictions because they are nonflammable and low in toxicity. Freon-113 decomposes rapidly at high temperatures such as those associated with gas flames or electric heaters. Products of decomposition include halogen acids, phosgene, and free chlorine.[27] The test cell housing the Freon-113 facility had an air exhaust system which completely changed room air every two minutes. There were no gas flames in the room and the a.c. loop heaters operated at a relatively low temperature of about 500°F.

The thermal stability of Freon-113 depends upon its temperature and the presence of other materials. At 400°F the decomposition rate in stainless steel is less than

six percent per year. The loop was operated at temperatures around 270°F for only a few hours and decomposition was therefore negligible. The filter-dryer (Appendix B) was in service whenever the pump was operating to remove any small amounts of particulates, oil, or decomposition products.

Test Section

The main body of the horizontal test section as installed in the loop is shown in Figure 3. The test section was constructed of type 304 stainless steel; it included an unheated flow development section which extended into the upstream piping. The test section housed a rectangular flow channel 0.3 inch high, 0.75 inch wide, and 29.56 inches long. The equivalent diameter of the channel was 0.428 inch. The channel had a uniform heat flux ribbon of type 302 stainless steel shim stock 0.005 inch thick, 0.125 inch wide, and six inches long. The ribbon was located 21 inches downstream from the flow development section thus providing an unheated inlet length of 49 length to diameter ratios for turbulent flow development. The ribbon was positioned along the center of the bottom of the flow channel by a pedestal structure of type 304 stainless steel (Figure 4). The pedestal housed the 0.375 inch diameter nickel heater electrodes and Conax penetrations, a thermocouple assembly and Conax penetration, and

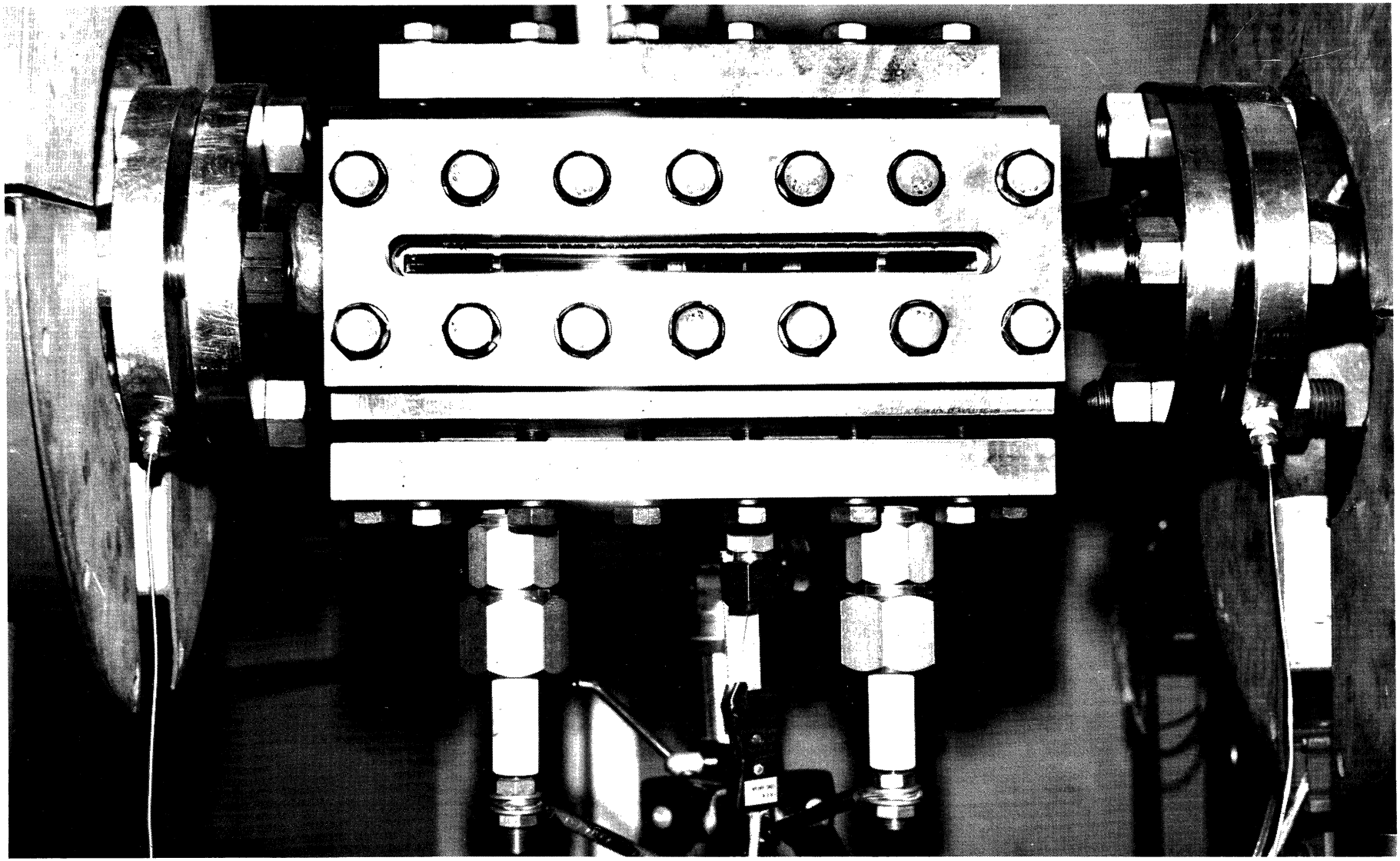

Figure 3. Test section installed in the loop. (Flow is from left to right.)

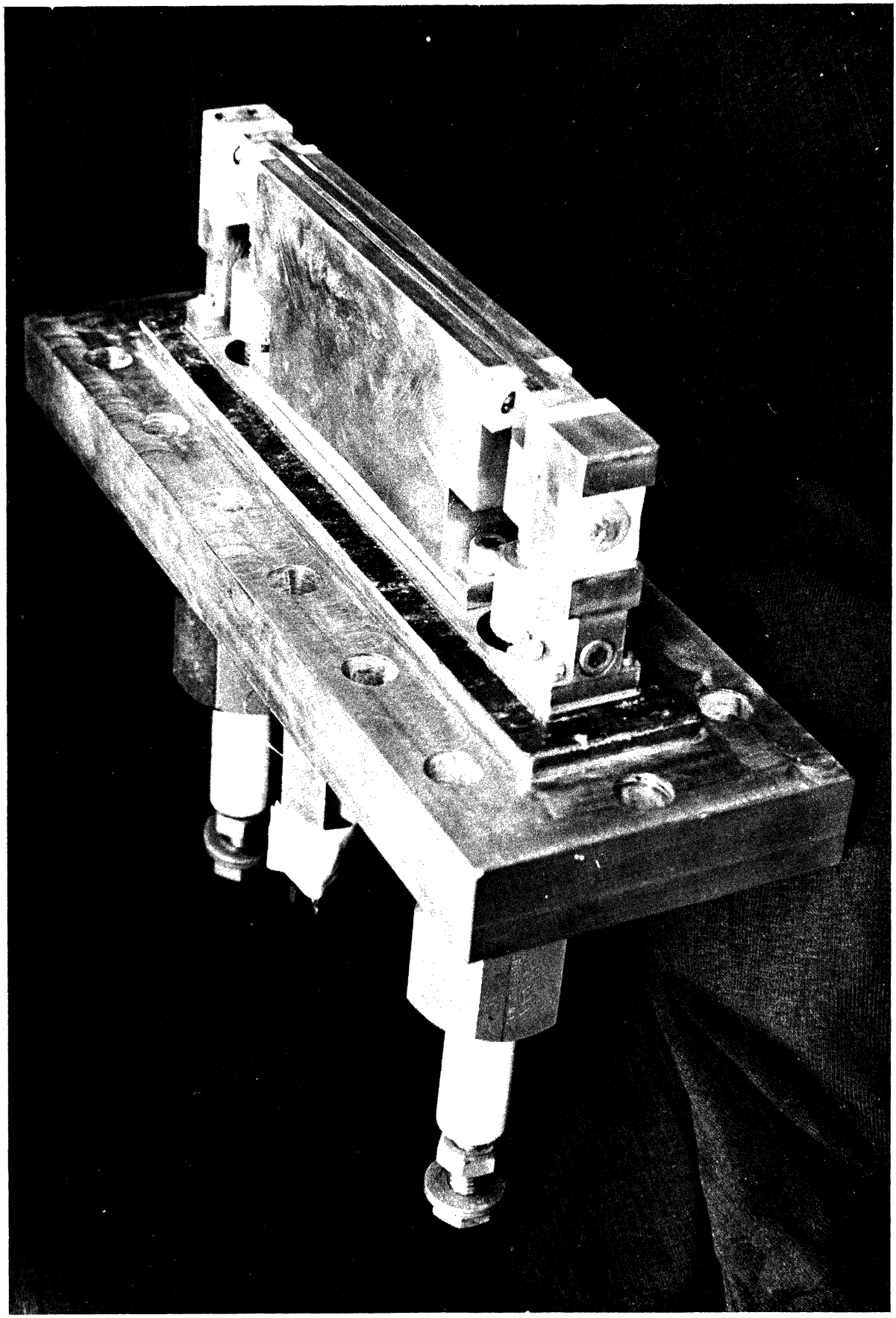

Figure 4. Ribbon heater pedestal removed from the test section.

a screw mechanism for pretensioning the ribbon at assembly. The latter allowed for thermal expansion of the ribbon without bowing. The ribbon and electrodes were insulated from the pedestal by lava spacers and Teflon seals. The ribbon was cemented to its lava insulator with Epoxylite 813. Direct current power was supplied to the ribbon by a 2400 watt silicon controlled rectifier.

The photographic side window assembly included a 0.75 inch thick pressure-retaining window of plate glass and a filler block of 0.625 inch thick float glass. There were no visible striations or inclusions in these two types of glass. The side windows were located to provide an unobstructed view of the flow channel over the entire ribbon heater length plus one inch at each end.

The side window assembly opposite the photographic window included a 0.75 inch thick pressure-retaining window of pyrex glass and a filler block of 0.625 inch thick float glass. The pyrex glass was obtained from a liquid level gage supplier and had parallel striations which prohibited high resolution photography through this window, but which did not affect diffuse back lighting of the flow channel. Similarly, the top window assembly, consisting of a 0.75 inch thick pyrex pressure-retaining window and two filler blocks of 0.75 inch thick plate glass,

was suitable for diffuse side lighting of the channel, but not for high resolution photography.

The filler blocks defined the channel geometry over the heated length. They were held in place by two 1/8 inch wide springs of 0.010 inch thick stainless steel. They were located just beyond each end of the heated length. The springs contacted the three glass sides of the flow channel but did not touch the bottom surface of the channel.

The pressure-retaining windows and the heater pedestal were sealed with 0.06 inch thick, neoprene-bonded asbestos gaskets. Each window had two gaskets--one on the inside surface which provided the seal and an identical gasket at the outside surface which cushioned the glass from the bolted window holders.

Instrumentation

(The instruments summarized here are described in more detail in Appendix B.)

Test section flow rate was measured with a calibrated orifice plate. Loop and test section pressures were manifolded to a 400 psi Heise gage. Coolant temperatures at the test section inlet and outlet were measured with 24-gage iron-constantan thermocouples. The ribbon heater temperature was measured with a grounded 38-gage

iron-constantan thermocouple mounted in contact with the back (non-boiling) side of the ribbon, approximately 0.5 inch from the downstream end. Ribbon voltage was measured outside of the test section across the 0.375 inch diameter nickel electrodes. The ribbon current was measured with a precision shunt calibrated at 50 mv per 100 amps.

The ribbon thermocouple and the ribbon voltage were used for DNB detection. At DNB, the output of the thermocouple increased at about 250°F/sec. The ribbon voltage signal also increased at DNB due to the resistance change of the ribbon as its temperature increased. The d.c. power supply adjusted automatically to load changes because it was operated in the current limiting mode. It thus maintained constant ribbon current throughout a DNB transient.

Temperature, power, and camera synchronization signals were recorded on a Honeywell Visicorder oscillograph. Ribbon temperature and voltage were recorded by low sensitivity, high frequency response galvonometers, while coolant temperatures and ribbon current were recorded by high sensitivity, low frequency response galvonometers. The ribbon thermocouple signal was amplified prior to recording by a differential d.c. amplifier with high common mode rejection. Figure 5 was traced from a typical oscillograph record of a DNB transient.

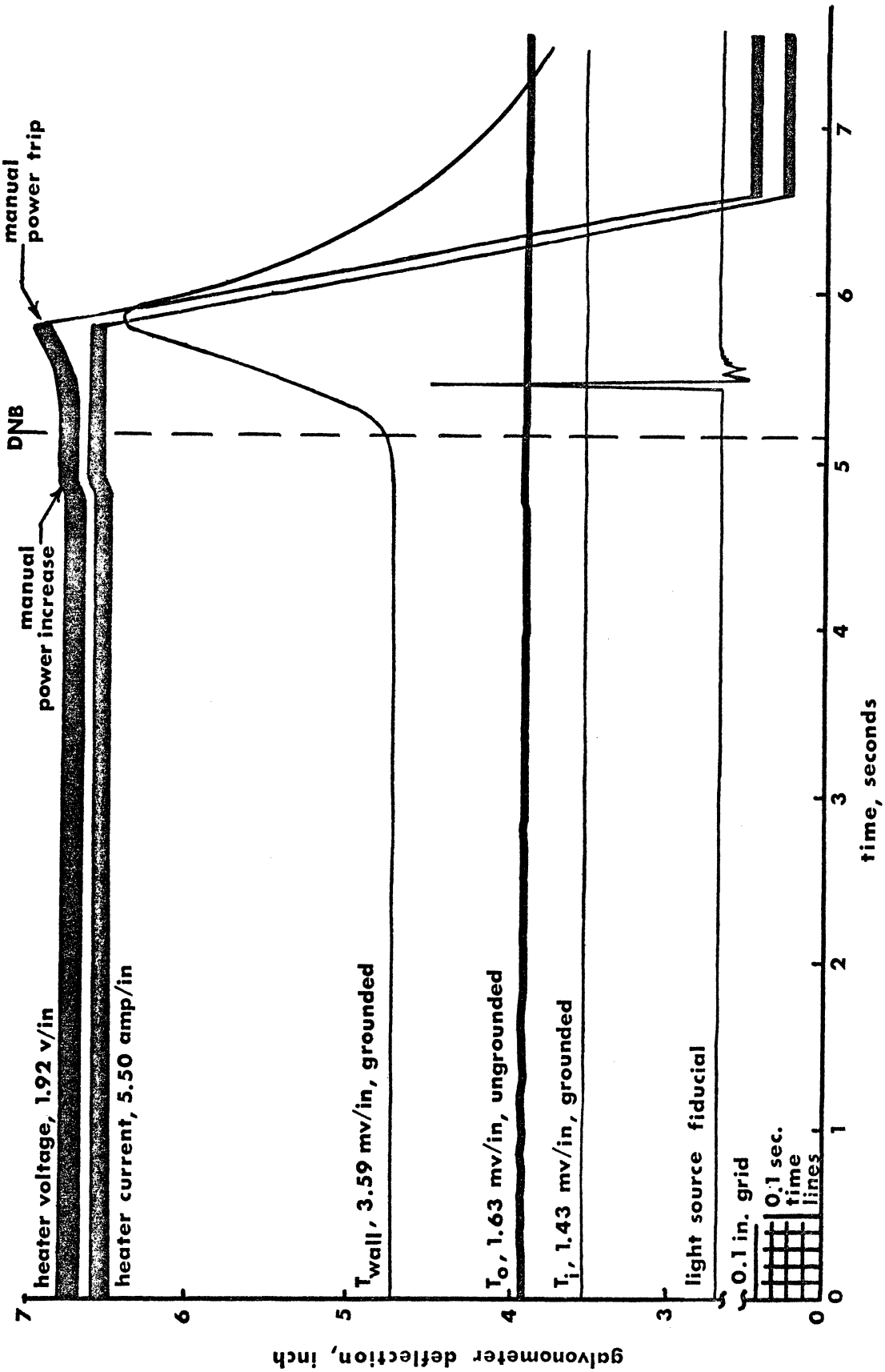

3350

Figure 5. Tracing of a typical oscillograph record.

Chapter 3

PHOTOGRAPHY

General

Resolution was the most important requirement in the design of this photographic study. Photographic resolution concerns the ability to discern small objects in relation to their surroundings. The aspects of a photographic system which influence the ability to obtain high resolution are: (1) contrast of the photographed object relative to its surroundings, (2) lighting of the object, (3) resolving power of the lens system at small apertures, (4) reproduction ratio of the lens system, (5) resolving power of the film, (6) grain size of the film, (7) enlarging capabilities of the film, (8) contrast capability of print paper, (9) contrast and resolution of the film developer. All of these factors were considered and optimized in this study to produce high resolution, readable photographs.

Of the factors listed above, the reproduction ratio (image size/object size) of the lens system was the key to high resolution photographs in this research. To illustrate the influence of this factor, consider a typical 35 mm still camera with a 50 mm focal length lens. This lens can focus on any object between about two feet and

infinity. As the camera is brought near to the object, the object's apparent size increases as the field of view decreases. At the closest distance for which the camera can focus, an 8 inch by 12 inch field of view is reduced to a 0.9 inch by 1.4 inch frame of film; i.e., the reproduction ratio is about 1:8.6. The resolving power of the camera as measured by the ability to resolve closely spaced, parallel lines would be about 1250 lines/inch (50 lines/mm). If the object were a 0.010 inch diameter bubble, it would occupy a 0.0012 inch diameter area on the film. Multiplying this diameter by the resolving power gives the size of the bubble relative to the smallest area which can be defined on the film. In this case the ratio is 1.5:1. Certainly there would be no discernable detail (such as shape) in such a photograph. The example given here is a relatively large bubble for the conditions of this research and therefore a better photographic system had to be devised.

The solution to this problem was to increase the reproduction ratio. This was accomplished by special lenses which focused on closer objects and by extension rings or bellows extensions between the camera and lens to permit focusing at object distances shorter than the image distance. Lens configurations and reproduction ratios used in this research are listed in the following section according to camera type.

As the reproduction ratio was increased the following changes occurred in the system: the field of view became smaller, the depth of focus was shortened, and the working distance between the lens and object was shortened. These factors directly influenced the design of the photographic test section and the kind of photographic data obtained. For example, because of the small field of view it was necessary to photograph only a short length of the ribbon heater. In this study, the camera was positioned so the field of view was at the downstream end of the ribbon where DNB was known to occur for an axially uniform heat flux. Because of this restriction no photographs were obtained which showed the bubble boundary layer over the entire length of the ribbon. Similarly, because the cameras had very narrow depths of field it was necessary that the ribbon heater be narrow to prevent clouding of the photographs by out-of-focus bubbles flowing in front of or behind the focal plane. Finally, the test section housing was designed to provide a minimum working distance between the camera lens and the ribbon heater consistent with the structural design requirements of a high-pressure facility.

A second factor which influenced the resolution of the photographs in this research was the exposure time; this factor was important because of the rapid movement

of the bubbles being photographed. Consider a bubble moving at 120 inches per second--a typical average axial velocity in the test section. If the exposure time is 10 microseconds, then the bubble moves a distance of 0.0012 inch during the exposure. If the negative is then enlarged and printed or projected at 25 times real size, the line which defines the edge of the bubble will be spread over a distance of 0.030 inch. To the naked eye this gives the appearance of a vapor cloud rather than a distinct vapor bubble. Longer exposure times would result in obvious vapor streaks on the film. This bubble clouding phenomenon was detected in still photographs lit by a General Radio Strobotac light source with a measured flash duration of 4.5 microseconds. Subsequent still photographs lit by a 1.2 microsecond flash unit showed distinct bubble images and had excellent resolution--0.0005 inch diameter bubbles were discernable in 25 x enlargements for flow velocities as high as 15 feet per second.

These two factors, reproduction ratio and exposure time, are fundamental to any photographic recording. They have been emphasized here because they were found to be the deciding factors in achieving excellent photographs of very small bubbles under flow, pressure, and heat flux conditions never before seen with such detail.

The reader interested in further details concerning high speed motion photography should consult references 28 and 29.

Equipment

The photographic systems used in this research are detailed in Table 2. A few figures of merit are included in the table to indicate the relative advantages of each system. The three systems were used to obtain three types of records: (1) still photographs of highest possible resolution to show detailed character of the bubbles and the bubble boundary layer, (2) motion pictures of relatively slow frame rate to record the complete DNB transient on film suitable for motion projection, and (3) motion pictures of high frame rate to show details of motion in the bubble boundary layer at times very near DNB.

Various locations and arrangements of the light sources were tried. The criterion for selecting the optimum conditions was the quality of bubble definition on or near the heated wall. Diffuse back lighting through the side window opposite the camera provided much better bubble definition on the heater than diffuse side lighting through the top window of the test section. Diffuse lighting was obtained by placing either a piece of ground glass or vellum paper between the light source and the test section.

Camera-Film Size	Lens	a	b	c	d	e	f	Light Source	Film and Developer	Resolution Limit
Nikkormat 35 mm (full frame)	55 mm, f/3.5 micro Nikkor reversed on Nikkor extension bellows	1.8	3.0	0.48 x 0.75	0.08	still	1.2	EG&G #501 stroboscope with FX3 lamp	Kodak Tri-X Panchromatic, D-76	0.0005 in. at 25x enlargement
Fastax WF1 8 mm on 16 mm film	101 mm, f/3.5 with 4 inch extension tube	1.16	15.8	0.12 x 0.37	0.08	6000 *	1.2	EG&G #501 stroboscope with FX3 lamp	Kodak Tri-X reversal, commercial processing	0.001 in. at 20x enlargement
Dynafax 16 mm on 35 mm film	75 mm, f/2.8 with 0.75 in. extension ring	0.22	16.3	1.1 x 1.7	0.12	25,000	1.05	Kemlite xenon arc lamp with custom built power supply	Kodak Tri-X Panchromatic, D-76, D-19	0.002 in. at 4.5x enlargement

a. Reproduction ratio, image/object
b. Closest focus, inch
c. Field of view, inch x inch
d. Depth of field, inch
e. Maximum frame rate, pictures/second
f. Exposure time, microseconds
* Limited by light pulse rate

Table 2. Photographic equipment

It was important to have good definition of the heater location in the photographs in order to make measurements of bubbles and bubble motion in this region. This was controlled by camera angle; several angles were tested under conditions of no heat flux and with low heat flux pool boiling. Camera angles which were too high above the horizontal plane produced a dark background for a thin region immediately above the heater. This occurred because light reflected from the bottom of the test section behind the ribbon underexposed the film in relation to the direct light reaching the film from the channel region high above the heater. Camera angles at or below the horizontal plane produced photographs which appeared fuzzy at the heater because of light reflections at the interface between the glass windows and the bottom of the flow channel. A slight camera angle of about 3° above horizontal resulted in optimum definition with the heater appearing in profile on the horizon between the brightly back-lit channel area and the dull, reflectively lit bottom surface of the channel. Fixed camera angle and position were maintained throughout the photographic data runs by sturdy camera tripods.

Photographs were scaled from the known 0.3 inch height of the flow section. This scale was checked against the measured frame sizes and fields of view of each camera at

the focus distances used. In addition, photographs of single phase convection or low heat flux boiling were a valuable aid to interpretation of the near wall region in photographs taken with identical camera placement but with intense vapor formation. These clearer photographs were also used in determining the heater location below its thin dark vapor blanket in post DNB photographs.

Chapter 4

PROCEDURE

The procedure for bringing the facility up to test conditions was as follows. The main loop was filled with liquid Freon-113 by admitting 20 psig air to the top of the storage tank. Air was bled from instrument lines and high points in the main loop during this filling process. The 6.5 kw a.c. clam shell heaters were turned on and allowed to heat up to a temperature preset on the Partlow controllers. Heating the Freon-113 from 70°F to 250°F required about eight hours; 16 hours was required to reach 270°F. As the Freon expanded during heatup the loop pressure increased. To prevent overpressurizing the loop, it was necessary to periodically open a valve in the return line between the main loop and the storage tank. The loop contained a 400 psi spring-loaded safety valve as backup protection against overpressurization.

Once the desired operating temperature was reached, the pump was started and the test section flow rate was adjusted by a combination of upstream and downstream throttling and pump speed adjustment. Test section pressure was then adjusted with the regulated compressed air supply to provide the desired operating pressure.

Boiling data and photographs were taken in the following manner. Ribbon power was turned on and manually incremented upwards. The Visicorder was used to record ribbon current, voltage, and temperature, and coolant inlet and outlet temperatures. Test section flow and pressure were read and recorded at each power level. Still photographs were taken at various power increments to record development of the bubble flow pattern at the downstream end of the heater. When ribbon voltage and temperature signals began to increase abruptly, thus indicating DNB, the power was reduced manually and then returned carefully to just below the CHF. A final still photograph was then taken. A DNB transient was initiated and terminated by manual operation of the power supply. Still or motion pictures were manually initiated to precede, coincide with, or follow DNB. It was usually possible to manually shut down the power supply without melting the ribbon, however, several ribbons did melt during the course of this research. Melting was localized and always occurred precisely at the downstream electrode. No further damage occurred to the test section due to ribbon melting. Black carbon deposits from local decomposition of Freon-113 were found on all melted ribbons.

High-sensitivity Visicorder channels were calibrated before each series of data collection runs with a Leeds and Northrup model 8686 potentiometer. The low sensitivity heater voltage channel was calibrated with an oscilloscope. The zeroes of all Visicorder channels were noted each time the instrument was used.

Chapter 5

RESULTS

Parameter Ranges

Critical heat flux data for subcooled flow boiling were obtained over the following range of parameters:

Pressure	148 to 334 psia
Exit Subcooling	50 to 112°F
Mass Flow Rate	1.16 to 3.19 x 10^6 lb/hr-ft^2
Heat Flux	1.68 to 3.06 x 10^5 Btu/hr-ft^2

The CHF data are given in Table C.1 of Appendix C. The error analysis in Appendix D assigns accuracies to these parameters.

Still photographs and Dynafax motion pictures of a quality suitable for space and time interpretation were obtained over the following range of parameters:

Pressure	105 to 352 psia
Exit Subcooling	39 to 119°F
Mass Flow Rate	1.23 to 4.10 x 10^6 lb/hr-ft^2
Heat Flux	0.27 to 3.01 x 10^5 Btu/hr-ft^2

Table C.2 lists the values of these parameters for the photographs which were used in the data reduction described below. On the basis of equal liquid to vapor

density ratios (see Appendix A) the pressure range of these photographs was equivalent to a water pressure range of 800 to 2400 psia. These are the only photographs known which reveal detailed information about the structure and behavior of the subcooled flow boiling regime at these high pressures and high mass flow rates.

Measurements were taken from a total of 56 still photographs and seven sets of Dynafax motion pictures. In addition, four 16 mm Fastax movies were used for qualitative viewing of bubble flow behavior near the heated surface. The Fastax movies were not used for frame-by-frame analysis because of the poor timing accuracy associated with the variable framing rate of this camera.

Figures 6 through 11 were selected as typical of the 56 still photographs used in the data analysis. Many more photographs were taken than were analyzed. The bases for selecting the 56 photographs were: (1) broad parameter range, (2) high optical quality, and (3) minimal duplication of data.

Figures 12 and 13 were selected from two sets of Dynafax motion pictures. Dynafax photographs were taken either shortly before or shortly after DNB but always before ribbon power was shut down. Each set of photographs contained about 150 frames covering a total time interval of 0.006 second.

Flow is from right to left in each of Figures 6 through 13. The axial location of the thermocouple on the back of the heater is marked by an x in these figures. The top of the channel in the still photographs has been artificially emphasized during the enlarging process for clarity in this publication. A small piece of epoxy located off to the side of the heater is seen on the right-hand side of the photographs in Figures 7-10. This epoxy did not interrupt the flow on the heater but it did hide a short length of heater in these photographs.

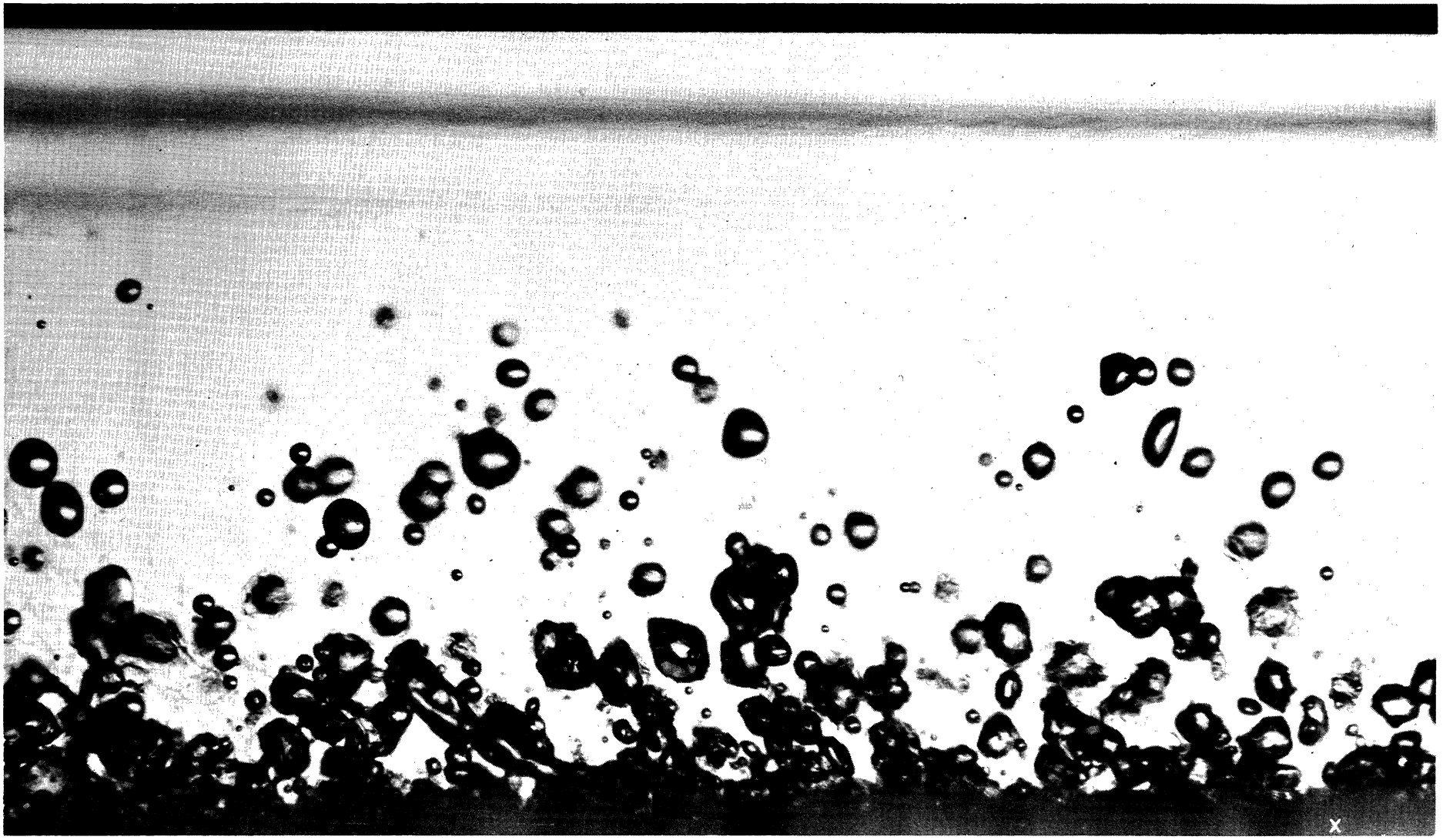

Figure 6. Still Photograph 18-6, before DNB, Scale = 16.8, P = 152 psia, ΔT_{sc} = 53 °F, G = 1.97x10^{6} lb/hr-ft^{2}, q" = 1.12x10^{5} Btu/hr-ft^{2}.

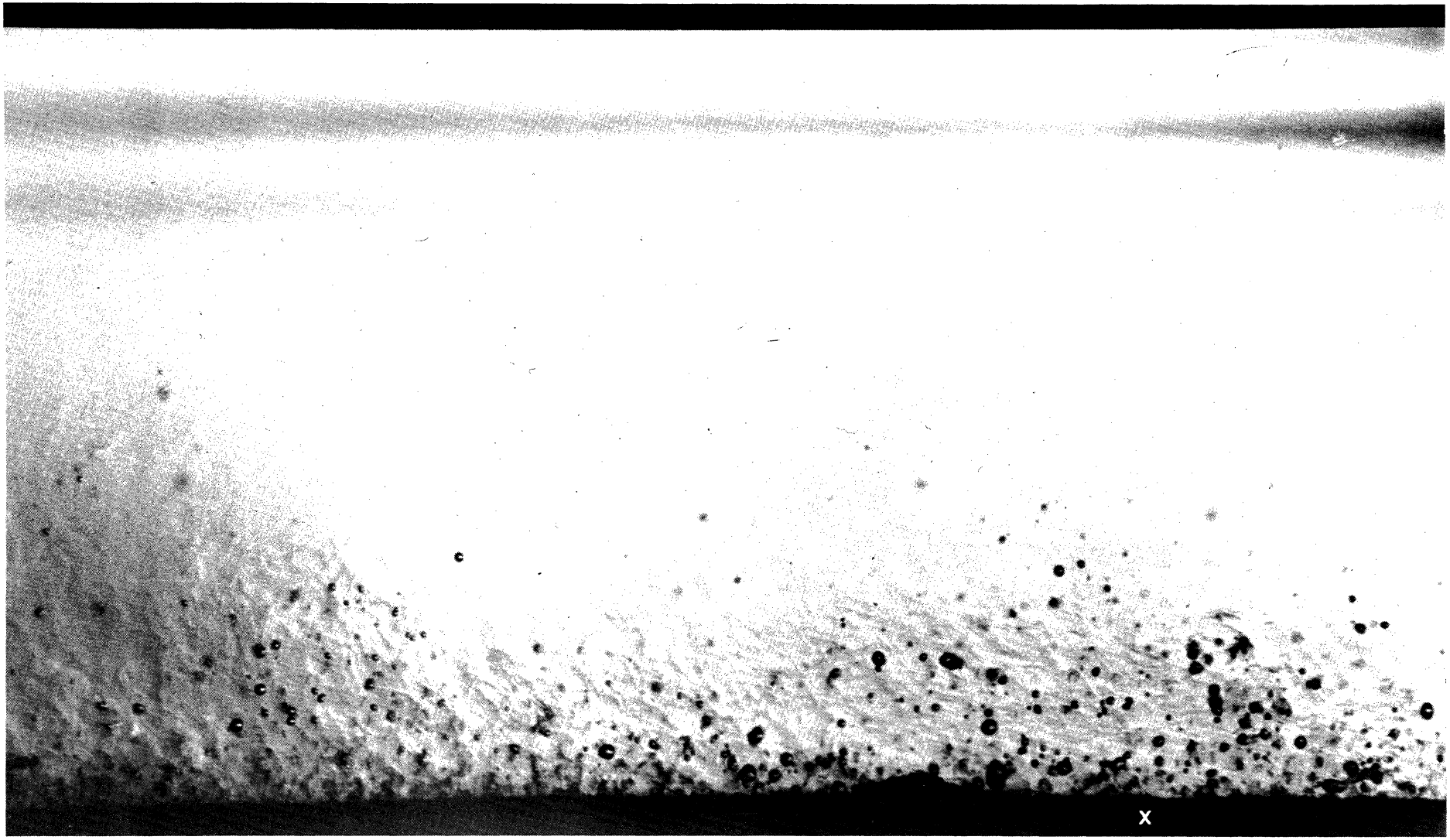

Figure 7. Still Photograph 21-14, before DNB, Scale = 16.8, P = 351 psia, ΔT_{sc} = 114 °F, G = 1.96×10^6 lb/hr-ft^2, q" = 1.11×10^5 Btu/hr-ft^2.

Figure 8. Still Photograph 19-15, before DNB, Scale = 16.8, P = 253 psia, ΔT_{sc} = 106 °F, G = 4.10×10^6 lb/hr-ft^2, q" = 2.42×10^5 Btu/hr-ft^2.

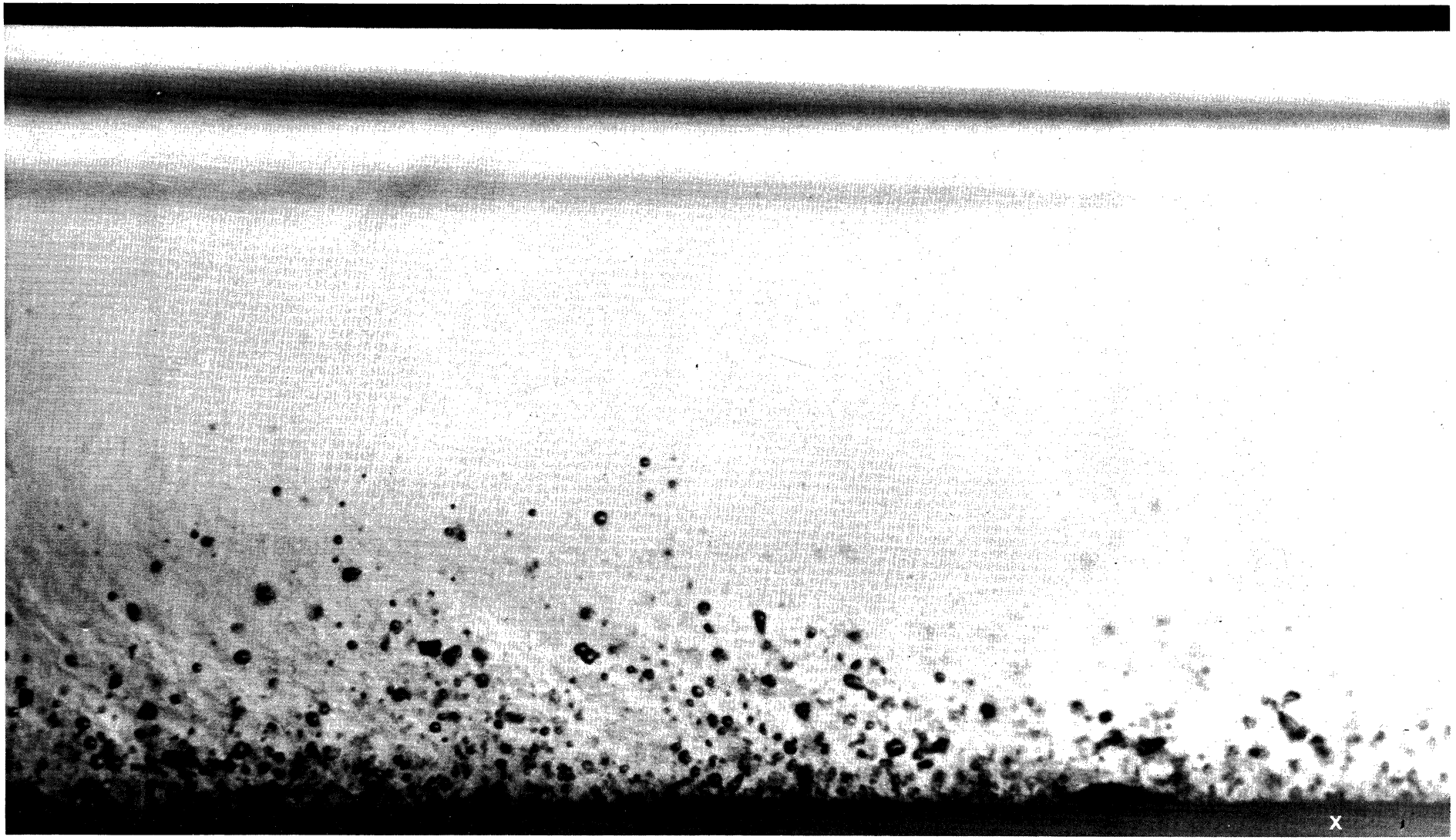

Figure 9. Still Photograph 19-8, before DNB, Scale = 16.8, P = 251 psia, ΔT_{sc} = 106 °F, G = 3.01×10^6 lb/hr-ft^2, q" = 1.69×10^5 Btu/hr-ft^2.

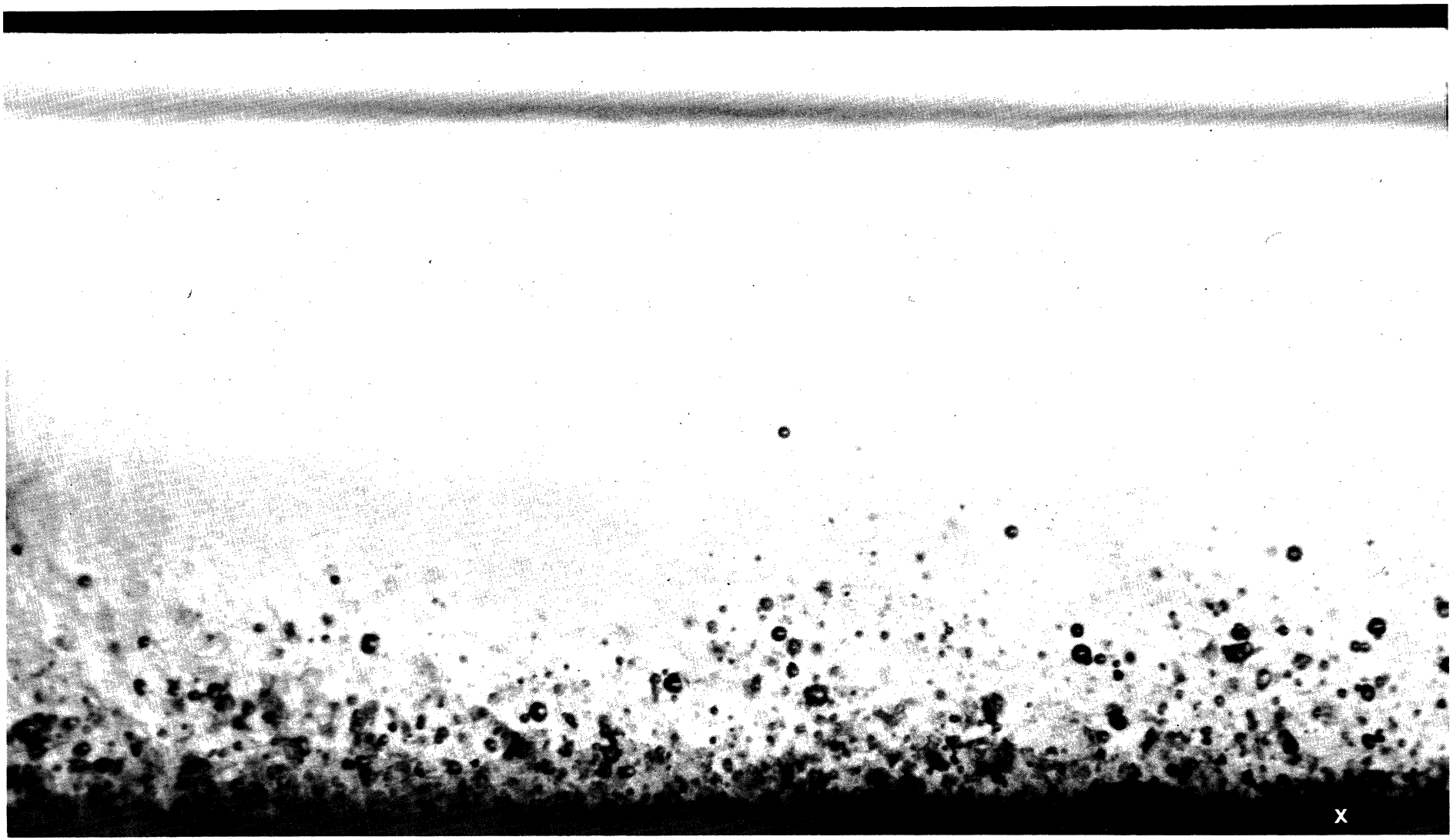

Figure 10. Still Photograph 19-9, before DNB, Scale = 16.8, P = 252 psia, ΔT_{sc}= 106 °F, G = 3.01×10^{6} lb/hr-ft^{2}, q" = 2.11×10^{5} Btu/hr-ft^{2}.

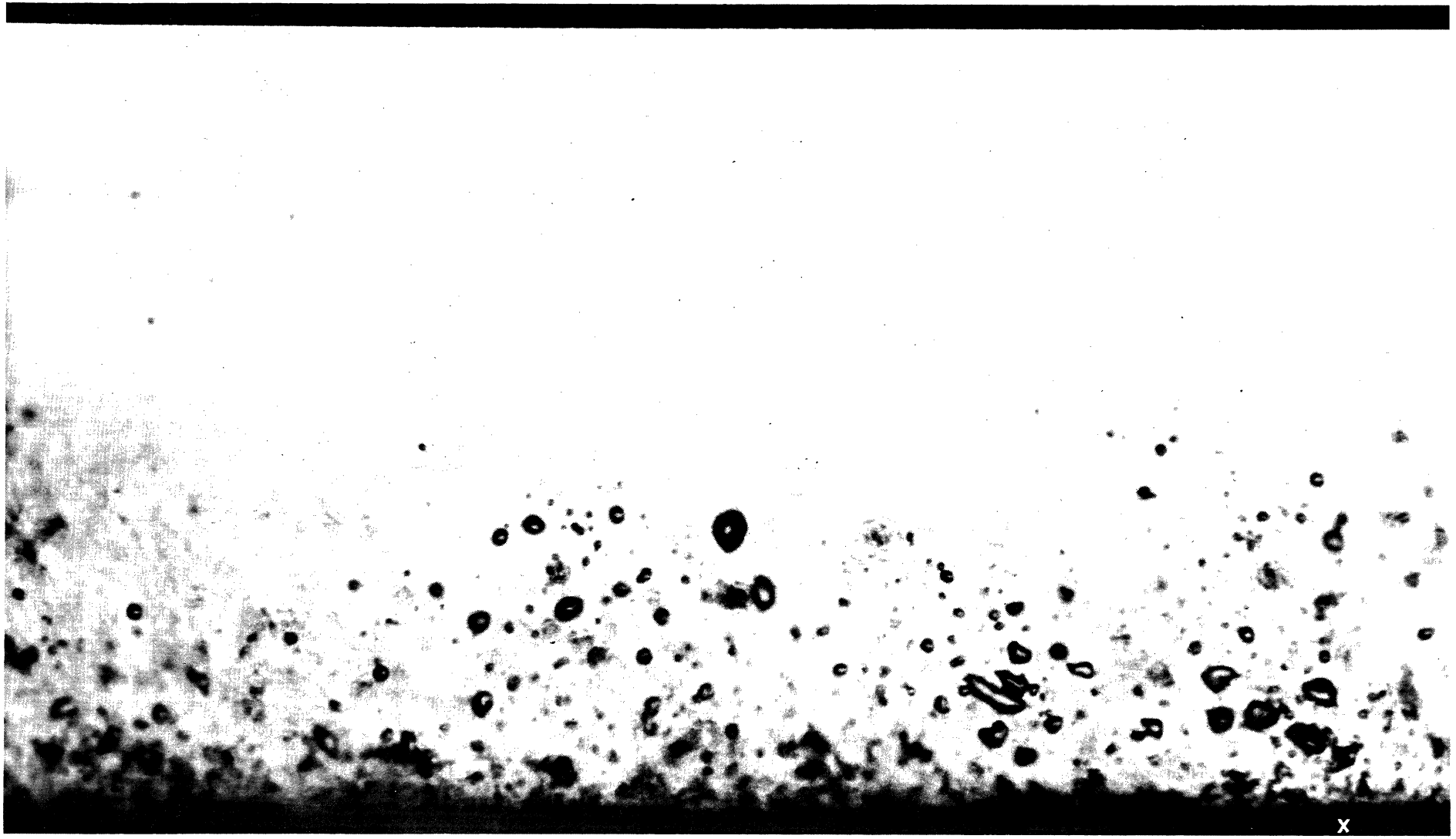

Figure 11. Still Photograph 19-10, at DNB, Scale = 16.8, P = 252 psia, ΔT_{sc} = 105 °F, G = 3.01x10^{6} lb/hr-ft^{2}, q''_{crit} = 3.01x10^{5} Btu/hr-ft^{2}.

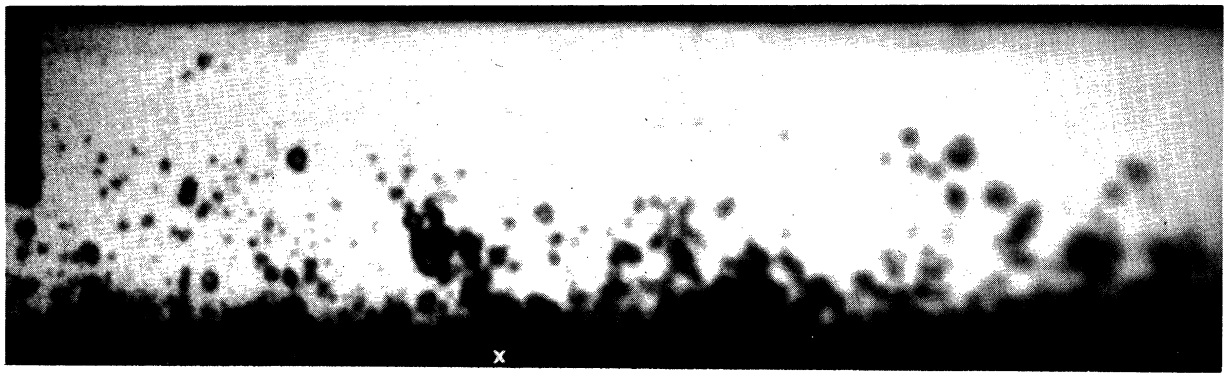

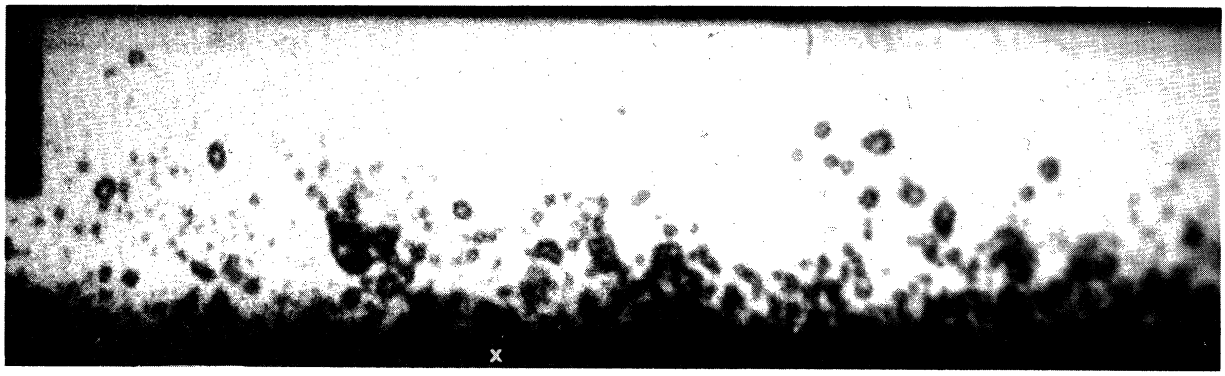

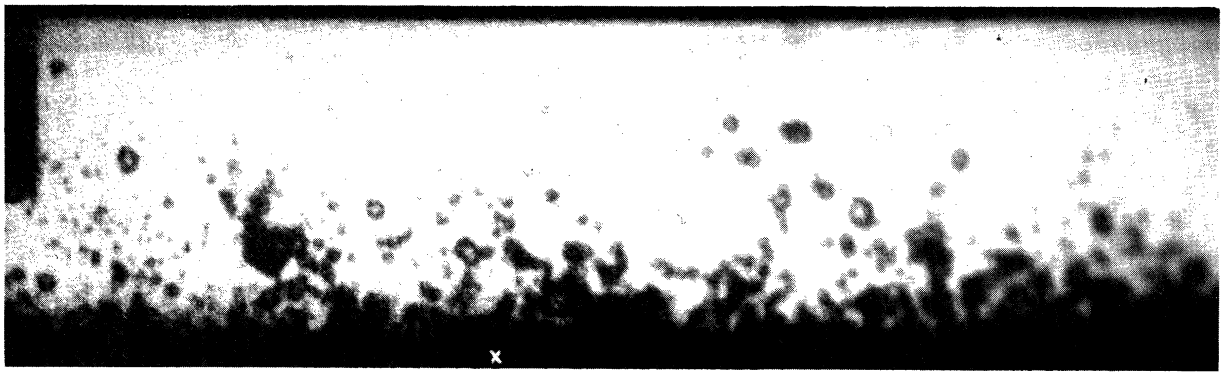

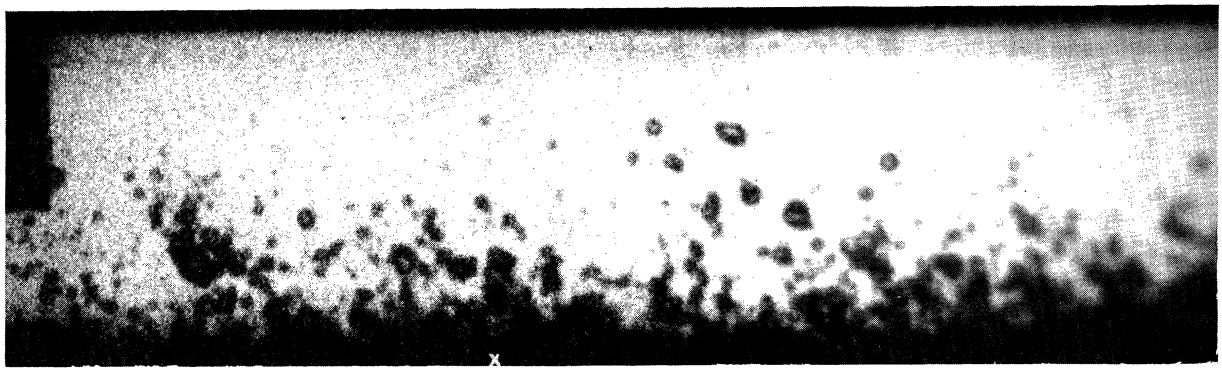

Figure 12. Dynafax Movie M9, every 20 frames, 0.25 second before DNB, Scale = 4.58, P = 308 psia, ΔT_{sc} = 105 °F, G = 2.02×10^6 lb/hr-ft^2, q''_{crit} = 2.20×10^5 Btu/hr-ft^2.

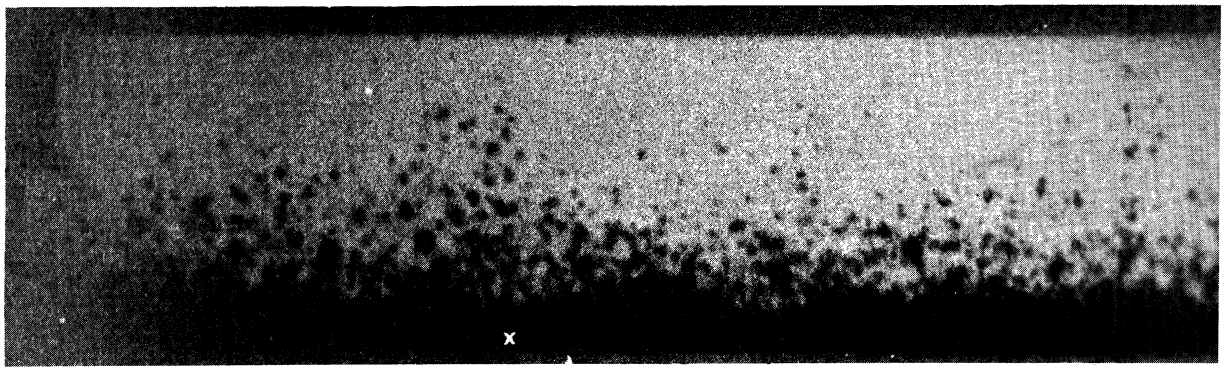

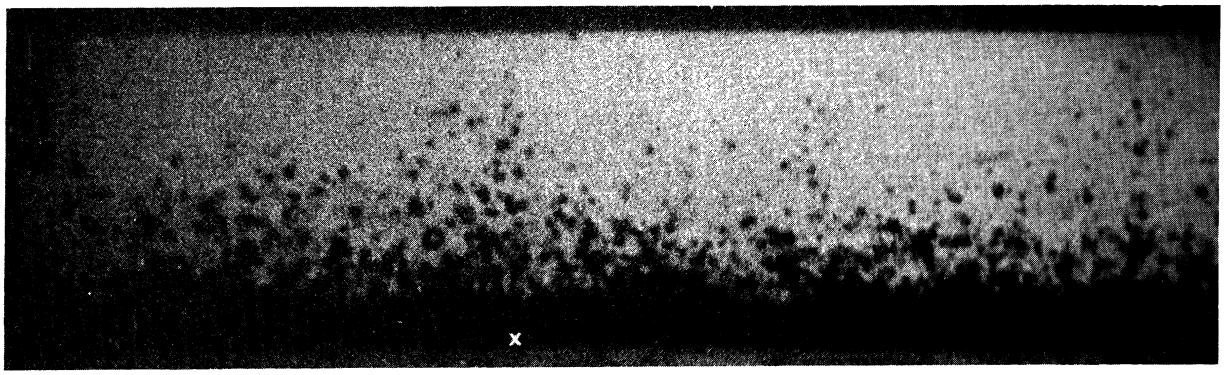

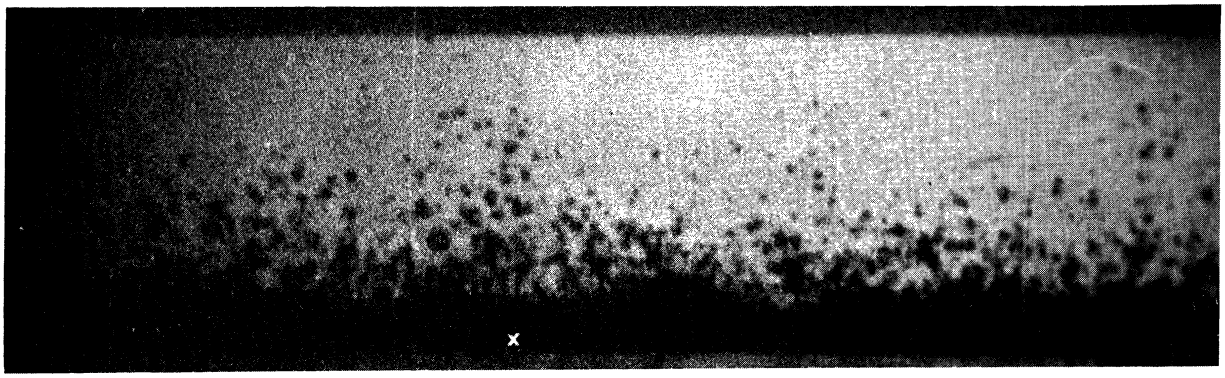

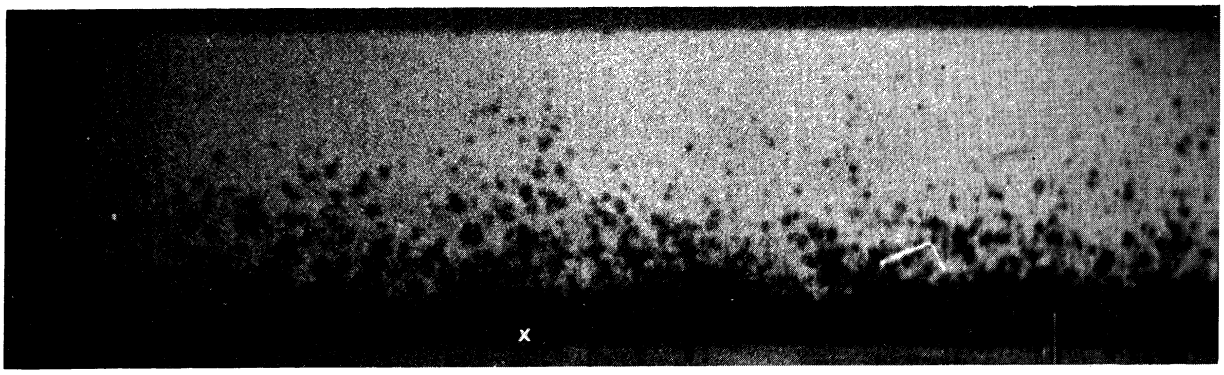

Figure 13. Dynafax Movie M13, every two frames, 0.01 second after DNB, Scale = 4.58, P = 325 psia, ΔT_{sc} = 110 °F, G = 3.19×10^6 lb/hr-ft^2, q''_{crit} = 2.82×10^5 Btu/hr-ft^2.

Critical Heat Flux Data

The critical heat flux data of Table C.1 were correlated by the following equation.

$$q''_{crit} = 2.7(h_{fg} + C_p\Delta T_{sc})G\left[\frac{\mu_l}{D_e G}\right]^{0.6}\left[1 + 1.25\,\frac{C_p\Delta T_{sc}}{h_{fg}}\right] \quad (1)$$

Figure 14 shows that the heat flux predicted by this equation was within ±30 percent of the measured CHF. Dean[10] developed equation (1) from the boundary layer separation model of DNB. He evaluated the empirical constants of equation (1) from DNB tests conducted with Freon-113 in an annular-geometry test section. Dean's CHF data are also shown in Figure 14; the correlations of that data and the present data by equation (1) were of comparable precision. This confirms that the ribbon heater and the two-dimensional flow channel used in this research provided adequate simulation of DNB in more common boiling heat transfer geometries.

The critical heat flux in Freon-113 was observed to be approximately a factor of 10 lower than the CHF for equivalent flow conditions in water. This scaling factor agrees with the consensus of heat flux scaling work described in Appendix A.

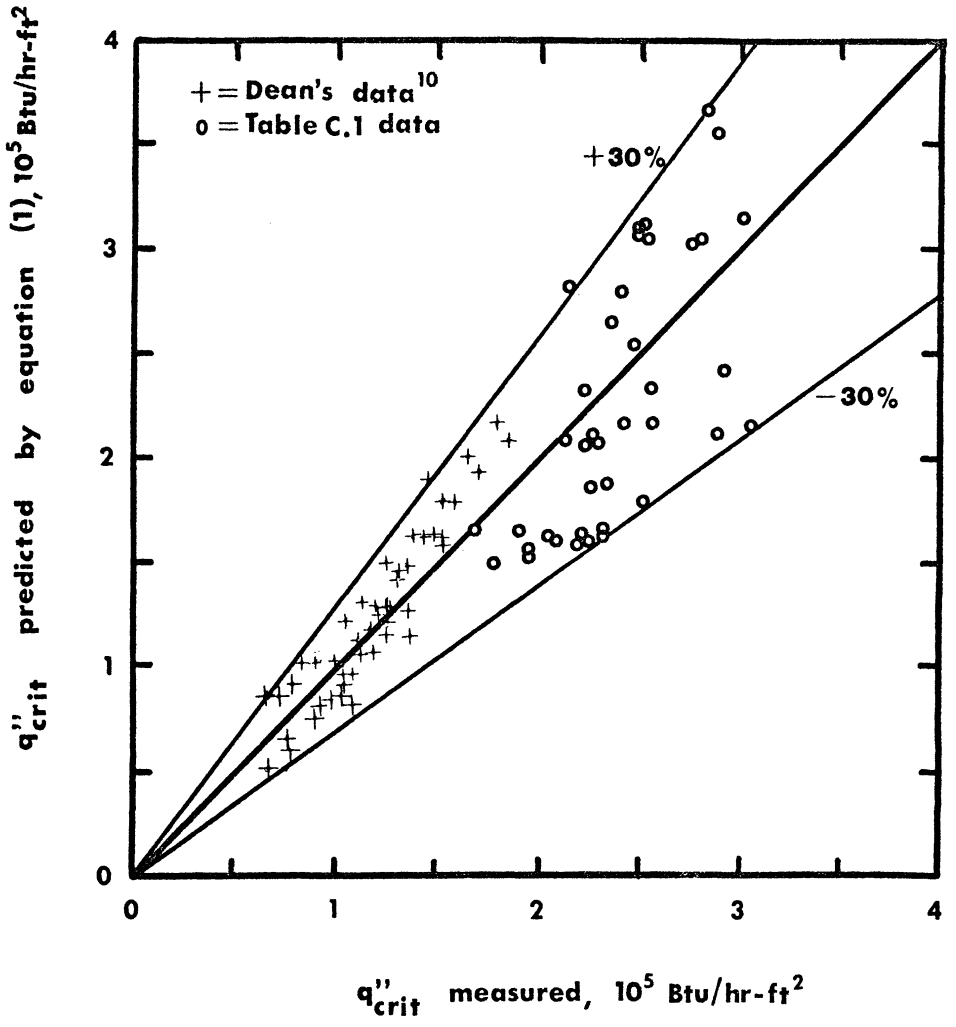

Figure 14. Correlation of critical heat flux data.

Bubble Size and Distribution

In this section some introductory comments are made regarding the general character of the bubbles observed in subcooled flow boiling; quantitative data obtained from the photographs are then presented and discussed.

This research was conducted at high pressures and high flow rates. The bubbles observed throughout most of the work were relatively small, were concentrated on the heated side of the channel, and did not coalesce sufficiently to form large slugs of vapor. This is the bubbly flow regime often discussed in the literature. One series of still photographs taken at 105 psia, 1.23×10^6 lb/hr-ft^2, and high heat flux showed large bubbles throughout the channel. A few of these were 0.1 inch in diameter, or, one-third of the channel height. At higher flow rates and pressures the bubbles were an order of magnitude smaller and were generally located below the vertical centerline of the channel (see Figures 6 to 13). The photographs at 105 psia were interpreted as an indication of the dividing line between (1) the subcooled slug flow at DNB in water below 90 psia, observed by Fiori and Bergles;[13] and (2) the subcooled bubbly flow at DNB in Freon-113 above 100 psia observed by Dean.[10] The 105 psia in Freon-113 is equivalent to 800 psia in water on the basis of the

scaling discussed in Appendix A. Further evidence that the subcooled slug flow regime at DNB may extend into the intermediate water pressure range was found by Styrikovich et al.[31] Using water they found average void fractions at subcooled DNB as high as 0.9 at 150 psia and 0.45 at 440 psia. Void fractions of this magnitude are more characteristic of slug flow than of bubbly flow.

In the present research bubbles growing on the heater were observed to move along the heater before departing into the subcooled liquid. Larger bubbles tended to move faster along the heater than smaller bubbles. Because of this velocity difference, large bubbles overtook smaller ones with the latter being absorbed to form a slightly larger bubble. The velocity difference can be explained by noting that larger bubbles extended further into the turbulent boundary layer, and the vapor high in the bubble was thus surrounded by liquid moving at much higher velocity than the liquid surrounding the bottom of the bubble. This imparted a tearing action which elongated the larger bubbles, pulling them away from the heater and in a downstream direction. Similar phenomena were reported in a photographic study by Treshchov[32] which was summarized by Tong, et al.[14] In subcooled flow boiling of water at pressures of less than 52 psia, bubbles were observed to

move along the surface immediately after they were formed. Treshchov also observed elongation of bubbles perpendicular to the surface as they grew larger and extended further into the turbulent boundary layer.

In the present research bubble size was observed to be a function of position relative to the channel wall. The bubbles coalesced on the heated surface and in the bubble boundary layer above the heated surface. The largest bubbles were located in the middle region of the bubble boundary layer. This phenomenon can be observed in Figures 6 to 13 and in the photographs of reference 14. Higher up in the bubble boundary layer the bubble size and population decreased because they condensed in the subcooled liquid.

Several kinds of bubble data were taken from the photographs listed in Table C.1 of Appendix C. These data were chosen to provide a description of the bubble behavior at DNB and a determination of the differences, if any, between bubbles below CHF and bubbles at CHF.

Measurements were made of the average diameter of the largest bubbles. These averages were called D_b and they are listed for each photograph in Appendix C. The ten largest bubbles in each photograph (or in one frame from a Dynafax set of photographs) were independently measured, scaled, and averaged by the author and an assistant. The results were

compared for consistency; where large discrepancies occurred the photographs were remeasured with more care in selecting the ten largest bubbles. When such discrepancies had been reduced to about 20 percent, the two averages for each photograph were again averaged and the result reported here as D_b. Several trials with 20 bubbles per photograph did not significantly change the value of D_b. The largest bubbles were chosen because: (1) large bubbles were easily identified, (2) the results provided a quantitative basis for comparing the maximum size of the bubbles with the bubble boundary layer thickness, and (3) this measurement provided quantitative proof that for the conditions of this research DNB was not caused or followed by the formation of large vapor slugs uncharacteristic of the bubbly flow regime.

This data was correlated by a computerized multiple linear regression analysis with a least squares fit criterion. Equation (2) is the dimensional correlation of the bubble measurements with the measured system parameters.

$$D_b = 559\ (p)^{-0.060}(\Delta T_{sc})^{-1.28}(G)^{-1.11}(q")^{0.992} \qquad (2)$$

These parameters were chosen because Tong, et al.[14] had previously used them to successfully correlate bubble departure size in low pressure subcooled boiling.

Correlated versus measured diameters were plotted in Figure 15; agreement was generally within ± 30 percent of the measured D_b. The coefficient of multiple correlation was 0.983. The average diameters of the largest bubbles in DNB photographs are indicated by "+" marks in Figure 15.

Two preliminary conclusions were drawn from this data: (1) the largest bubbles at DNB were always relatively small compared either to the channel height or to the bubble boundary layer thickness (see Bubble Boundary Layer section); and (2) since equation (2) correlated both the DNB cases and the cases below CHF with the same precision, the flow pattern or flow mechanisms which limit bubble size did not change in this respect at DNB.

Another correlation of these bubble measurements in terms of the significant dimensionless groups is given in equation (3) which correlated the measured values within ± 30 percent as shown in Figure 16.

$$\frac{D_b p}{\sigma} = 5.91 \times 10^6 (St)^{1.06} (Pr)^{-0.431} \left[\frac{\rho_l}{\rho_v} - 1\right]^{-2.72} \left[\frac{\mu_l}{\mu_v}\right]^{3.82} \quad (3)$$

The coefficient of multiple correlation for equation (3) was 0.984. Thermal and transport properties in equation (3) were evaluated at the saturation temperature.

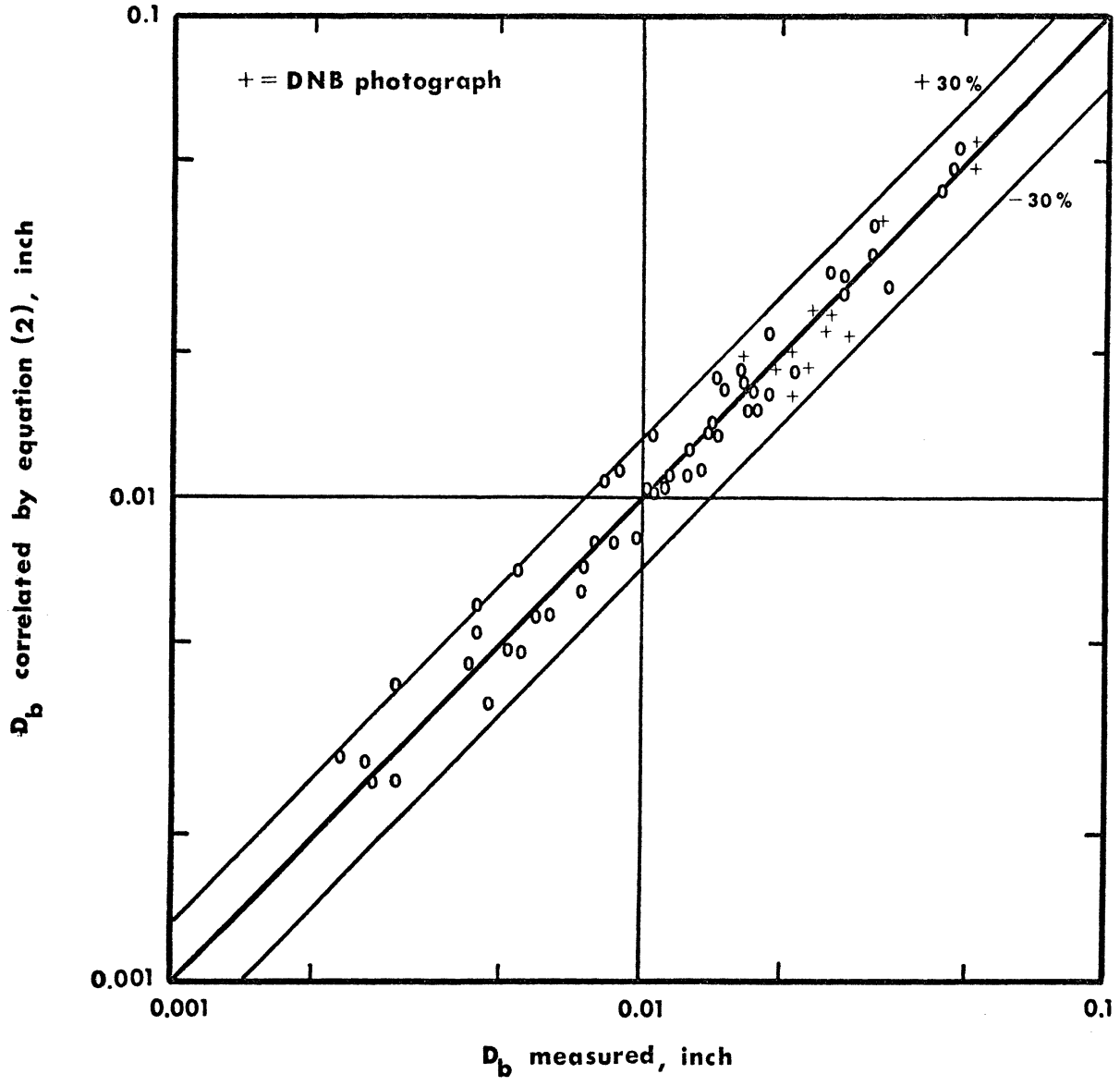

Figure 15. Dimensional correlation of average diameter of largest bubbles.

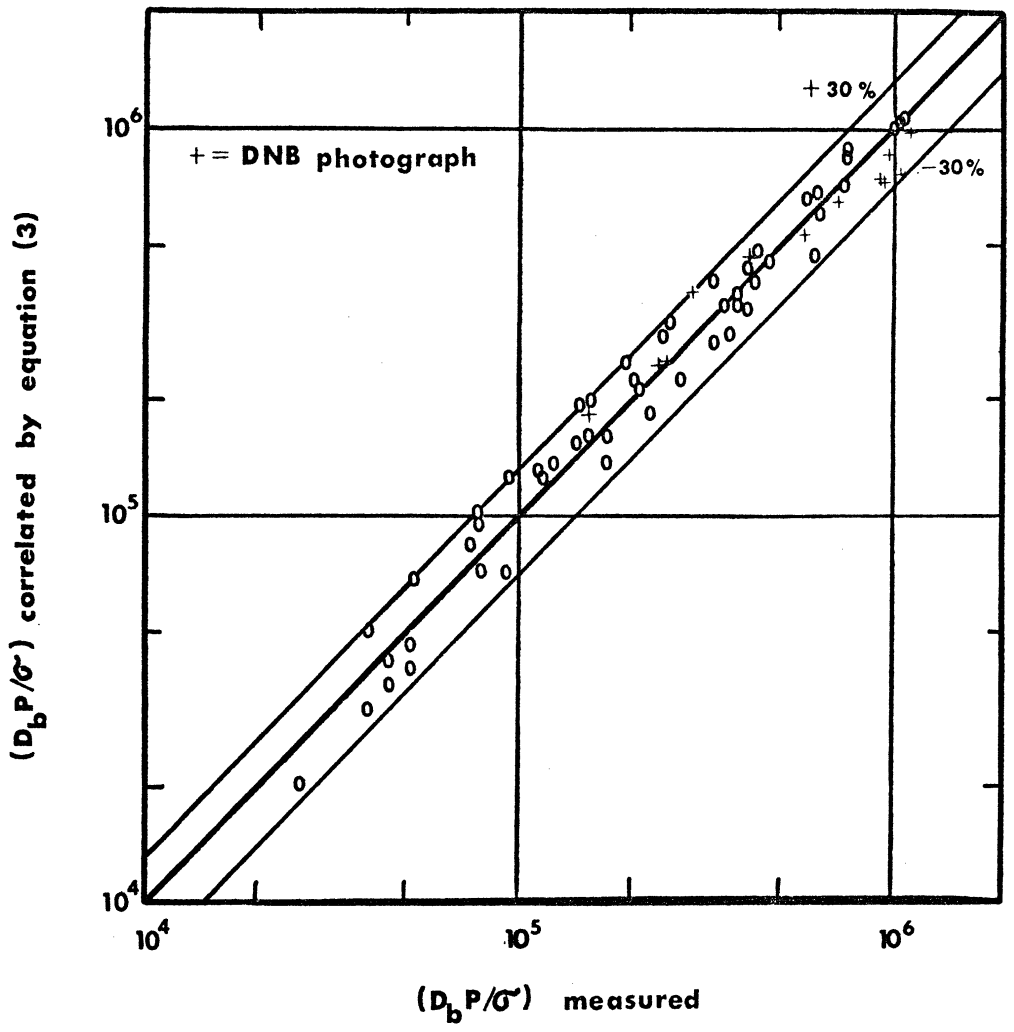

Figure 16. Nondimensional correlation of average diameter of largest bubbles.

Dimensional analysis was used to select the Prandtl, Weber, and Stanton numbers as correlating parameters. In addition, a total of 16 different nondimensional groups were systematically applied to the data. (Difficulty in dimensional analysis of the many parameters and properties affecting two-phase flow is discussed in Appendix A.) The parameter combinations of equations (2) and (3) provided the best fits to the measured values in terms of standard errors of estimate, multiple correlation coefficients, and standard errors of the regression coefficients.

The bubble size distribution and population density near the ribbon heater were measured from nine still photographs. The nine photographs were chosen to provide highest resolution in the 0.020 inch region above the heater and to cover a range in heat flux up to CHF. The procedure used was to (1) scale the photographs from the known channel height; (2) draw a line parallel to and above the heater by a distance of 0.020 inch times the scale; (3) select an area below this line which contained approximately 100 bubbles; (4) measure and scale all of those bubbles; (5) compute the bubble population density for the volume counted (volume = 0.020 x 0.125 x length); and (6) plot the normalized number of bubbles in each bubble size range. The author and an assistant performed these tasks independently for each of the nine photographs; discrepancies between the two independent measurements were negligible.

The region 0.020 inch above the heater was chosen for this measurement because (1) the region included bubbles at or near departure from the heater, (2) the region was slightly thicker than the vapor film observed in post-DNB photographs, and (3) the results provided a quantitative measure of change at the boiling surface as the boiling crisis was approached with an increase in heat flux.

The results of the measurements are illustrated in Figures 17, 18, and 19. In these figures the number of bubbles within selected small size ranges was divided by the total number of bubbles counted in a particular photograph and plotted against the bubble diameter. The bubble population density p.d. was also given for each of the nine photographs represented in Figures 17 to 19. The following observations were made with regard to these figures: (1) the largest bubbles (Figure 15) were larger than any of the bubbles in the 0.020 inch thick region near the wall; (2) the bubble size distribution grew wider as heat flux was increased; (3) the bubble population density first increased with increasing heat flux and then decreased because of coalescence before CHF; (4) the void fraction at the wall, being approximately equal to the product of bubble population density and mean bubble volume, increased with heat flux and was maximum at DNB; and (5) the bubble size distribution was narrower and the mean bubble size was smaller for higher mass flow rates.

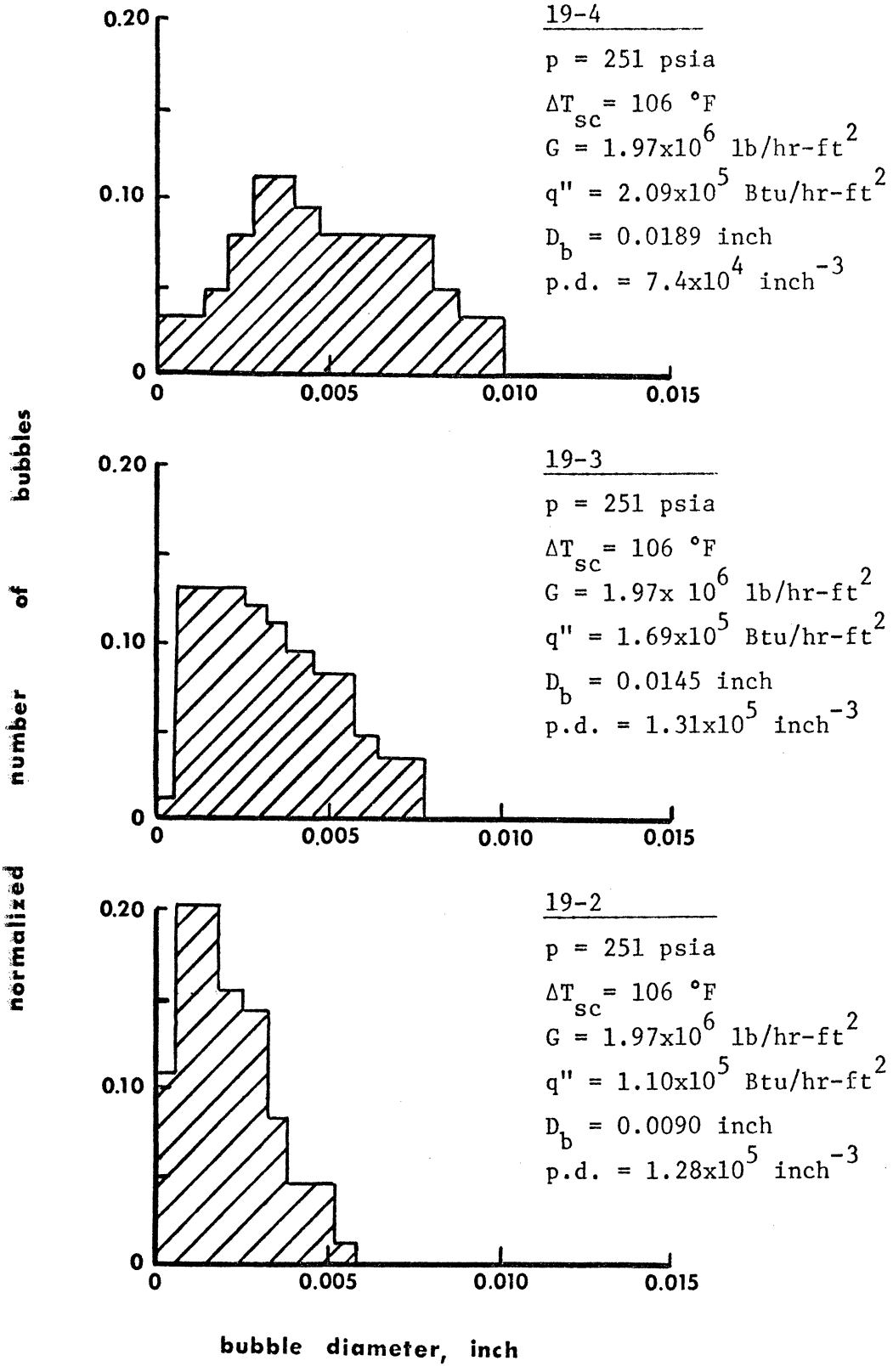

3362

Figure 17. Bubble size distribution and population density near the heated surface. Case 1.

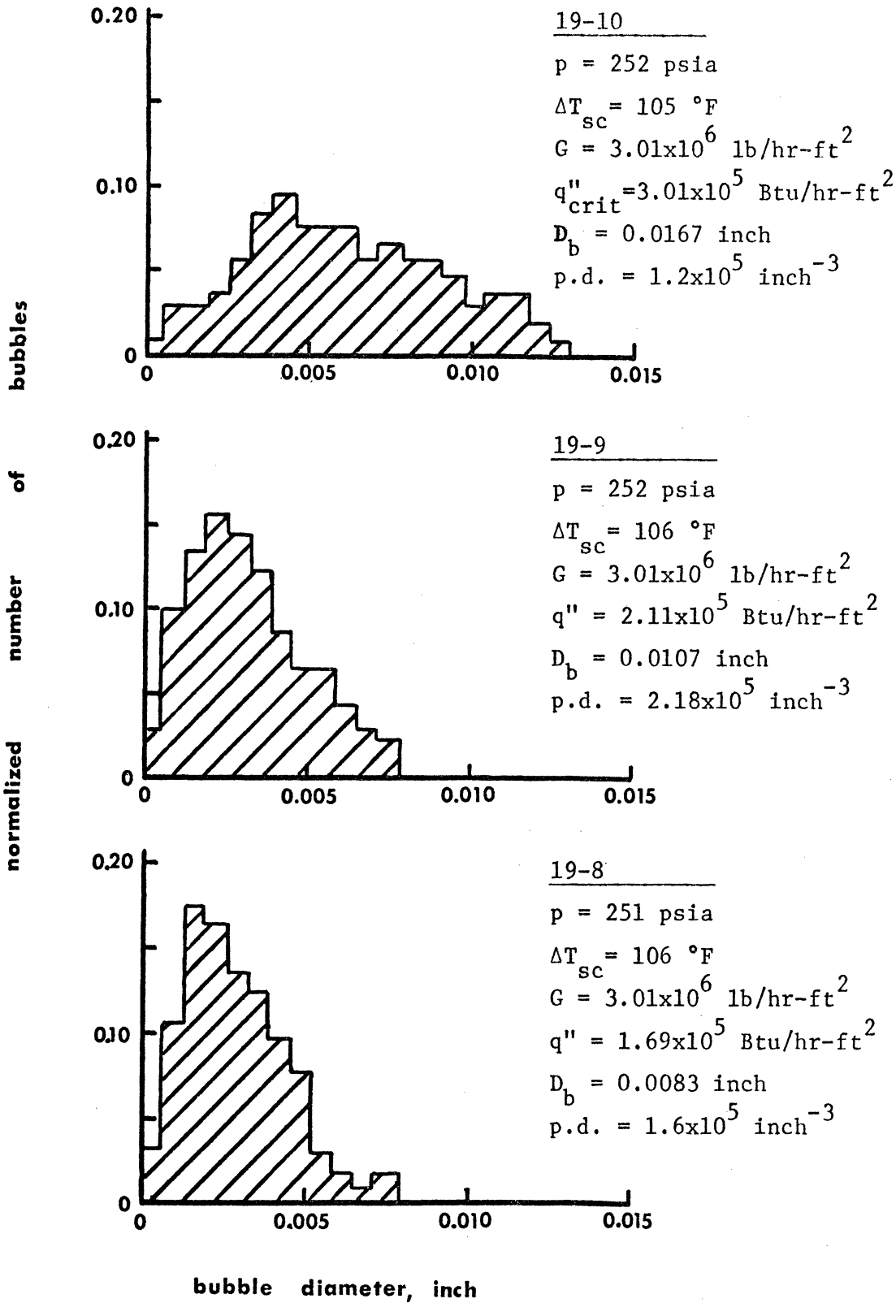

Figure 18. Bubble size distribution and population density near the heated surface. Case 2.

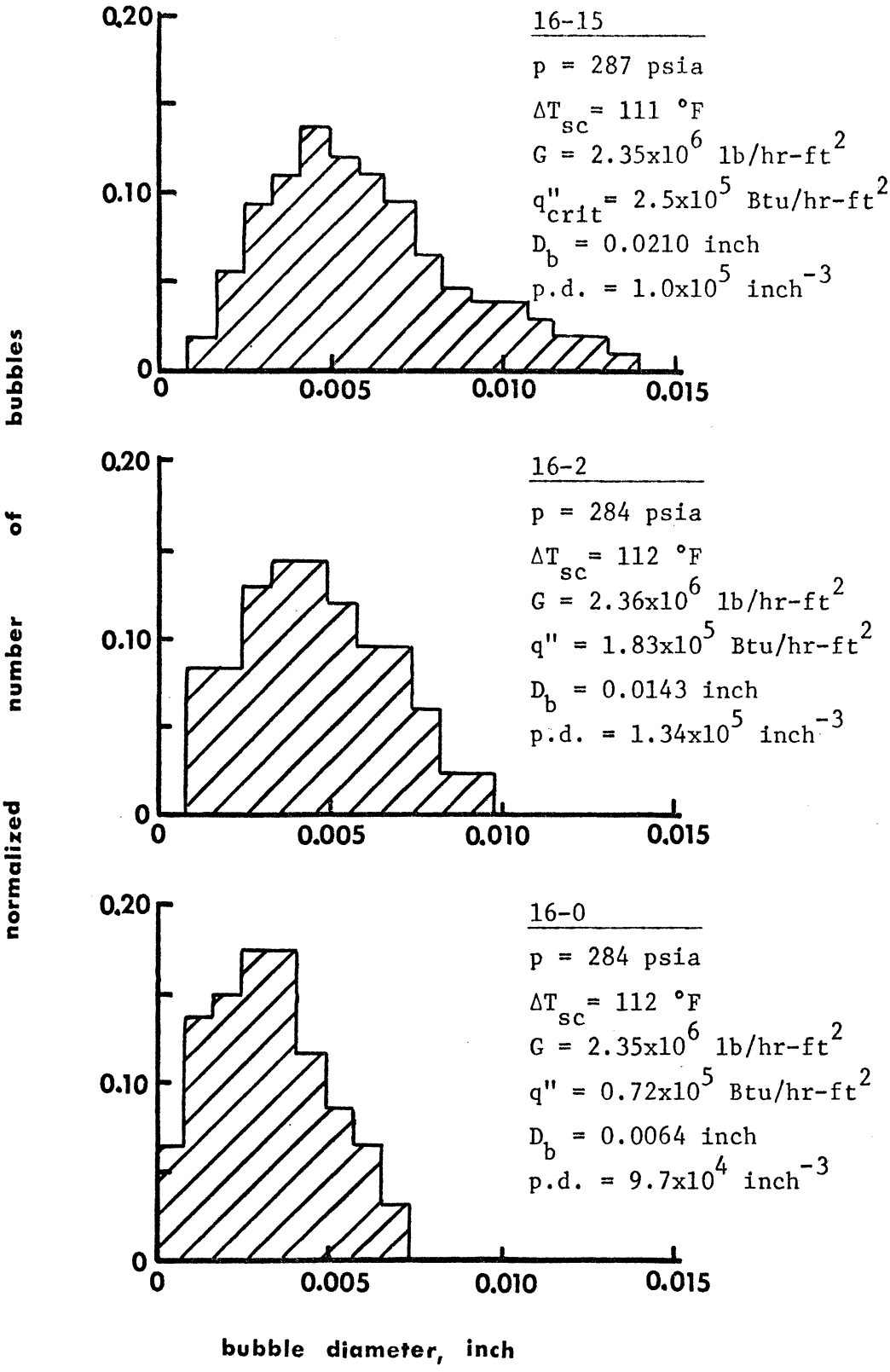

Figure 19. Bubble size distribution and population density near the heated surface. Case 3.

Void fractions are not reported here, and it should not be assumed that these measurements provided an accurate method for determining void fraction; the data was taken in only two dimensions. Both the in-focus and the out-of-focus bubbles, however, were considered in these measurements, thereby giving some credence to the qualitative insight offered by Figures 17 to 19. For example, it was known that void fraction near the wall increased as CHF was approached.[13, 31] The photographs obtained in this research and Figures 17-19, in particular, add to this knowledge by indicating the manner in which the void fraction increases. At low heat flux, increasing the heat flux caused slightly larger bubbles to be generated in greater numbers. This tendency was reversed before CHF where even larger bubbles were generated, but in smaller numbers because of coalescence. At CHF the bubbles were observed to spread out by joining with neighboring bubbles on the heater. In this way the bubbles assumed a flattened shape rather than a spherical shape, and they formed thin vapor clouds over the heater for distances as long as 0.07 inches (Figures 11 and 13 for example). These cloud formations continued to move along the heater and they were intermittently dispersed by vapor departure from the surface. This phenomenon was expected for the transition

boiling regime which follows DNB and in which there is intermittent film and nucleate boiling.

A comparison of the measurements of D_b in Table C.2 with Figures 17-19 shows that the largest bubbles in a particular photograph were larger than any in the region near the heater. Thus the largest bubbles resulted from bubbles coalescing after they departed from the heated surface. The largest bubbles were also fewer in number than the bubbles on the heater, as can be seen in Figures 6-13. It was concluded that the largest bubbles do not significantly affect the heat transfer mechanism or the boiling crisis mechanism because of their small population density and because of their position well above the heated surface.

Vapor Velocity

The axial vapor velocity as a function of distance from the heated wall was measured from Dynafax movies which were taken immediately before or after DNB. The method of data reduction was to (1) identify a particular bubble in an early frame of a movie, (2) track its motion through subsequent frames for as long as it remained clearly defined, (3) measure the distance traveled by the center of the bubble relative to the downstream window spring shown at the left-hand side of each frame, and (4) compute the axial velocity of the bubble from the

known frame rate of the camera. The error analysis in Appendix D assigns typical uncertainties of ± 2.0 percent to the measured vapor velocities. Bubbles high above the heater were easily tracked by observing every twentieth frame of a movie, as in Figure 12. Bubbles on or near the heater had to be tracked using every second frame, as in Figure 13, because they could not be identified for long periods of time. They changed shape rapidly and were quickly obscured or absorbed by neighboring bubbles. The 25,000 frames/second picture rate of the Dynafax camera was about twice as fast as was necessary to follow bubble growth and movement on the heater.

This data has been plotted in two ways in Figure 20. First, the axial velocity of a bubble was divided by the average single phase liquid velocity, which was calculated by assuming no vapor in the channel. This was plotted against the average vertical position of the center of the bubble for the time period it was tracked. Second, the vapor velocities were divided by the vapor velocity at the channel centerline and plotted against the average positions of the bubbles. The Nikuradse approximation for the single phase liquid velocity distribution, equation (4), was also plotted in Figure 20.

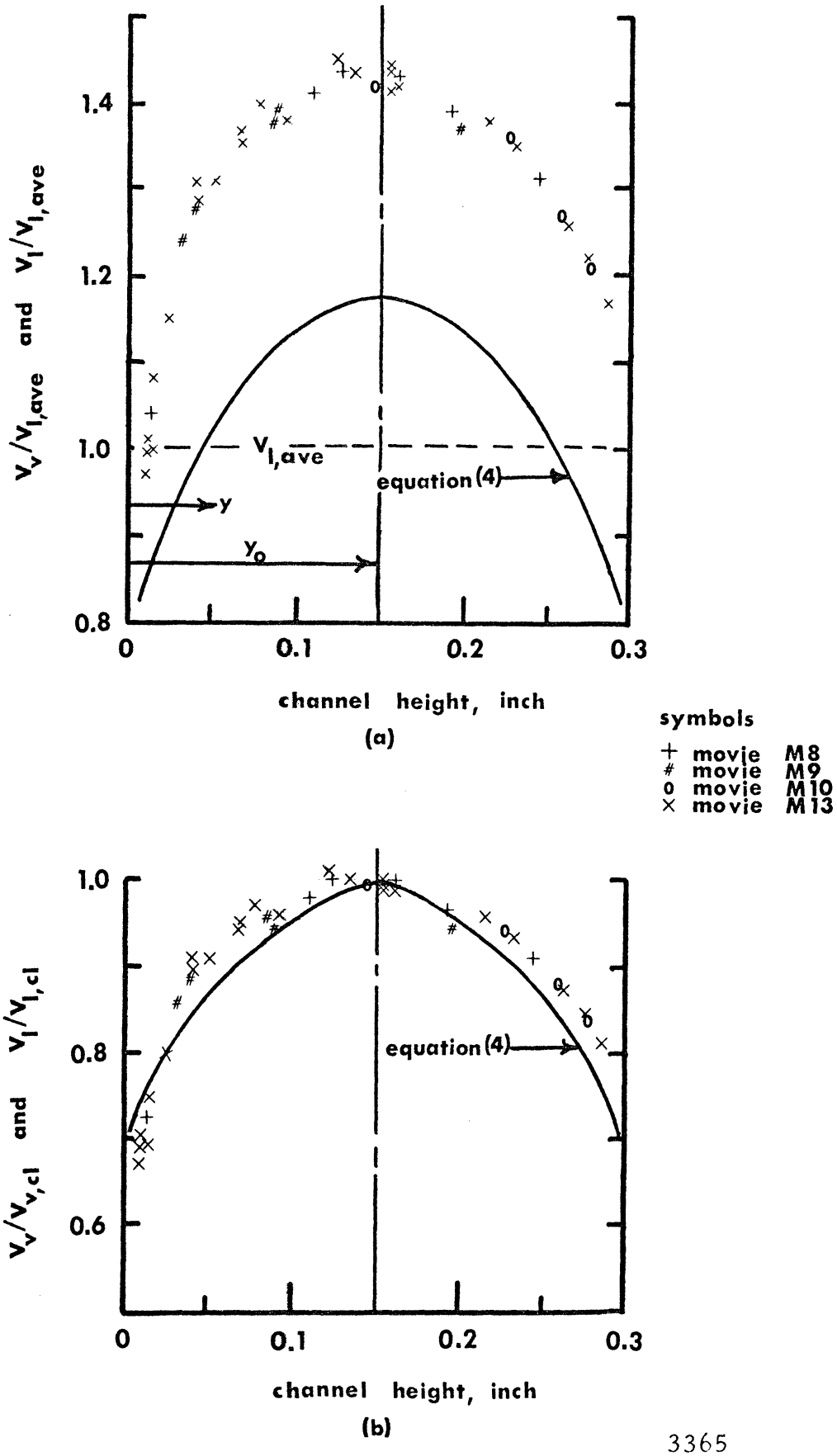

Figure 20. Axial vapor velocity at DNB.

$$V_l/V_{l,cl} = (y/y_o)^{1/8} \qquad (4)$$

This equation was developed for isothermal flow in circular pipes, but it has been found acceptable for flow between parallel plates.[33] The effect of diabatic flow is to steepen the velocity gradient near a heated surface because of local reduction of the liquid viscosity. The one-eighth power applies to a single phase Reynolds number of about 2.0 to 3.0 x 10^5, a range typical of the movies of Figure 20.

Assuming that the liquid velocity profile was that of equation (4), Figure 20 shows that the local slip ratio defined by

$$s(y) = V_v(y)/V_l(y) \qquad (5)$$

was greater than 1 over the entire channel except in the region 0.010 inch above the heater. In the Dynafax movies it was impossible to discern individual bubbles closer to the heater than 0.010 inch because of the intense formation of vapor in this region and the poor resolving power of this camera compared to the still camera.

The axial vapor velocity exceeds the liquid velocity because of what Tong[25] has called the "Bernoulli effect" in two-phase flow. The mechanism is simply that the less dense vapor phase accelerates faster than the more dense liquid phase when both are subject to the same static pressure

drop along the flow. Thus the vapor phase attains a higher velocity than the liquid phase.

It appears from Figure 20a that the volume average slip ratio was greater than 1 for the movies taken at DNB. This conclusion cannot be made without qualification because accurate void fraction measurements cannot be taken from two-dimensional photographs. The volume average slip ratio is given for this two-dimensional study by

$$\bar{s} = \frac{\int_{-y_o}^{y_o} bV_v(y)\alpha(y)\,dy}{\int_{-y_o}^{y_o} bV_l(y)[1 - \alpha(y)]\,dy} \qquad (6)$$

It is impossible to integrate this equation over the channel height without knowing the spatial dependence of the void fraction $\alpha(y)$. Thus the volume average slip ratio $\bar{s}$ has not been calculated here. Rose and Griffith[34] used air in water to show that for bubbly flow with volumetric flow concentrations $(Q_v/(Q_v + Q_l))$ greater than about 0.25, the volume average slip ratio can exceed a value of 1. This supports the conclusion from Figure 20a that the volume average slip ratio at DNB is greater than 1. With

lower heat flux and, hence, lower volumetric flow concentrations the vapor is all confined to a very thin region near the wall where the liquid velocity is low. Rose and Griffith found that when the volumetric flow concentration was less than 0.25 the volume average slip ratio was less than 1.

Figure 20b shows that the measured vapor velocity gradient near the heater is not as steep as the gradient predicted by equation (4), while the vapor velocity gradient at the unheated wall is approximately equal to equation (4). This results in a slight asymmetry of the vapor velocity profile. This phenomenon is explained as the converse of the mechanism described above in explaining why large bubbles on the heated surface move faster than small bubbles. That is, at high heat flux there are large bubbles on the heater which protrude beyond the region of high velocity gradient within the turbulent liquid boundary layer. Thus the bottoms of the bubbles are located in a very low velocity region while the tops of the bubbles are located in the high velocity liquid stream. Bubble continuity is maintained by the surface tension force. As a result, the large bubbles are pulled along the heater more rapidly than liquid moves near the heater. Conversely, bubbles are retarded from moving as fast as the free stream liquid as long as the bubbles are partially located within the region of high liquid velocity

gradient. This explains why the vapor velocity gradient is less steep than the liquid velocity gradient near the heated surface, where large bubbles are located. On the other hand, the velocity gradients are approximately equal at the unheated surface, where only tiny bubbles are found.

The vapor velocity perpendicular to the heated surface was also measured in Dynafax motion pictures. The vapor phase is lighter than the liquid phase, so the bubbles experience a buoyant force. Zuber and Findlay[35] gave the terminal vapor rise velocity for bubbly flow in a turbulent stream as

$$V_v(y) = 1.53 \left[\frac{g_c g(\rho_l - \rho_v)}{(\rho_l)^2} \right]^{1/4} \qquad (7)$$

The solution of this equation for Freon-113 at 250°F gives a terminal vapor rise velocity of 5.2 inches/second. This value was typical of the bubble rise velocities measured in regions of low bubble population high above the heated surface. A vapor rise velocity of 5.2 inches/second is large enough to explain the appearance of small bubbles at the top of the flow channel near the downstream end of the heater; these bubbles were generated at the upstream end of the heater. A few of them did not completely collapse while flowing above the heater and were carried to the top of the channel by the buoyant force.

In regions of high void fraction near the heater the bubbles had not yet accelerated to the 5.2 inches/second predicted by equation (7). Their vertical motion was also subject to interference from other bubbles and to coalescence. In addition, some bubbles were observed to move unsteadily away from the heater. Their upward motion was slowed or reversed briefly by the turbulent mixing of the subcooled liquid stream. Turbulent mixing was also observed by noting the rotation of some bubbles in relation to adjacent bubbles as they flowed through the test section.

Due to the high axial velocity of the liquid stream and the much smaller velocities associated with turbulent mixing, there were only slight variations in the axial velocities of the adjacent bubbles. No bubbles were found which flowed counter to the main stream flow. This is substantiated by Figure 20 which shows no discontinuities in the vapor velocity profile at DNB; thus, there were no vapor flow instabilities at DNB.

Bubble Boundary Layer

The thickness of the bubble boundary layer was measured from the 63 photographs listed in Table C.1 of Appendix C. Figures 6 to 11 show that in the still photographs the upper edge of the bubble boundary layer was sometimes uneven or interrupted by small clusters of very small

bubbles which had risen out of the bubble boundary layer by buoyancy and turbulent mixing. Figures 12 and 13 show that the greater perspective and the sequential photographs of the Dynafax movies removed the subjectiveness in this measurement by more clearly distinguishing the occasional clusters above the boundary layer. With the insight offered by the sequential Dynafax photographs and with some practice. a consistent, reproducible measurement technique was developed. A transparent straight edge was placed over the photographs and adjusted to coincide with a line encompassing all of the bubbles except for the occasional clusters of small bubbles described above. Measurements of the bubble boundary layer thickness were all made at 0.5 inch from the downstream end of the heater, i.e., the thickness δ tabulated in Table C.1 was measured above the heater thermocouple. The author and an assistant independently measured and scaled each of the photographs. The two measurements were compared for consistency and were repeated when disagreement was more than 10 percent. In Appendix D errors of $\pm$ 7 percent were estimated for the measurement of bubble boundary layer thickness.

This data was correlated by a computerized multiple linear regression analysis with a least squares fit criterion. Equation (8) is the dimensional correlation of the data.

$$\delta = 13.2(p)^{-0.113}(\Delta T_{sc})^{-0.410}(G)^{-0.486}(q")^{0.435} \qquad (8)$$

correlated versus measured thicknesses were plotted in Figure 21; agreement was generally within ± 30 percent of the measured δ, and the coefficient of multiple correlation was 0.909. The bubble boundary layer thicknesses in DNB photographs are indicated by "+" marks in Figure 21.

Two preliminary conclusions were drawn from this data: (1) the bubble boundary layer thickness at DNB was large compared to the size of the largest bubbles at DNB (Figure 15) or compared to the bubble sizes in the 0.020 inch thick region above the heater (Figures 17 to 19), and (2) since equation (8) correlated both the DNB cases and the cases below CHF with the same precision, the flow pattern or flow mechanisms which determine the bubble boundary layer thickness did not change in this respect at DNB.

Another correlation of the boundary layer measurements in terms of the significant dimensionless groups is given by equation (9) which correlated the measured values within ± 30 percent as shown in Figure 22.

$$\frac{\delta p}{\sigma} = 4.66 \times 10^{7}(St)^{0.490}(Pr)^{-0.644}\left[\frac{\rho_l}{\rho_v} - 1\right]^{-2.39}\left[\frac{\mu_l}{\mu_v}\right]^{2.41} \qquad (9)$$

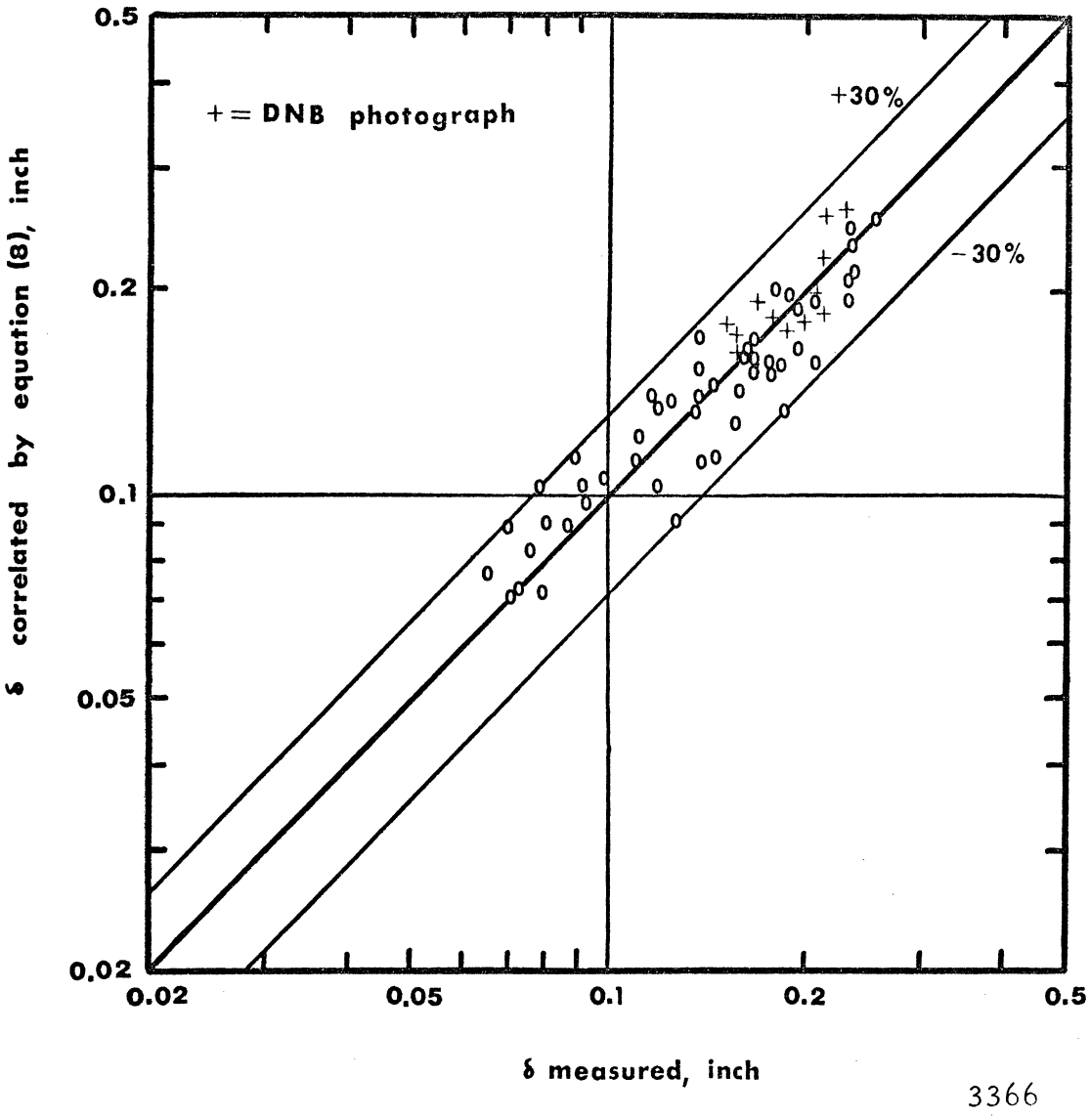

Figure 21. Dimensional Correlation of bubble boundary layer thickness.

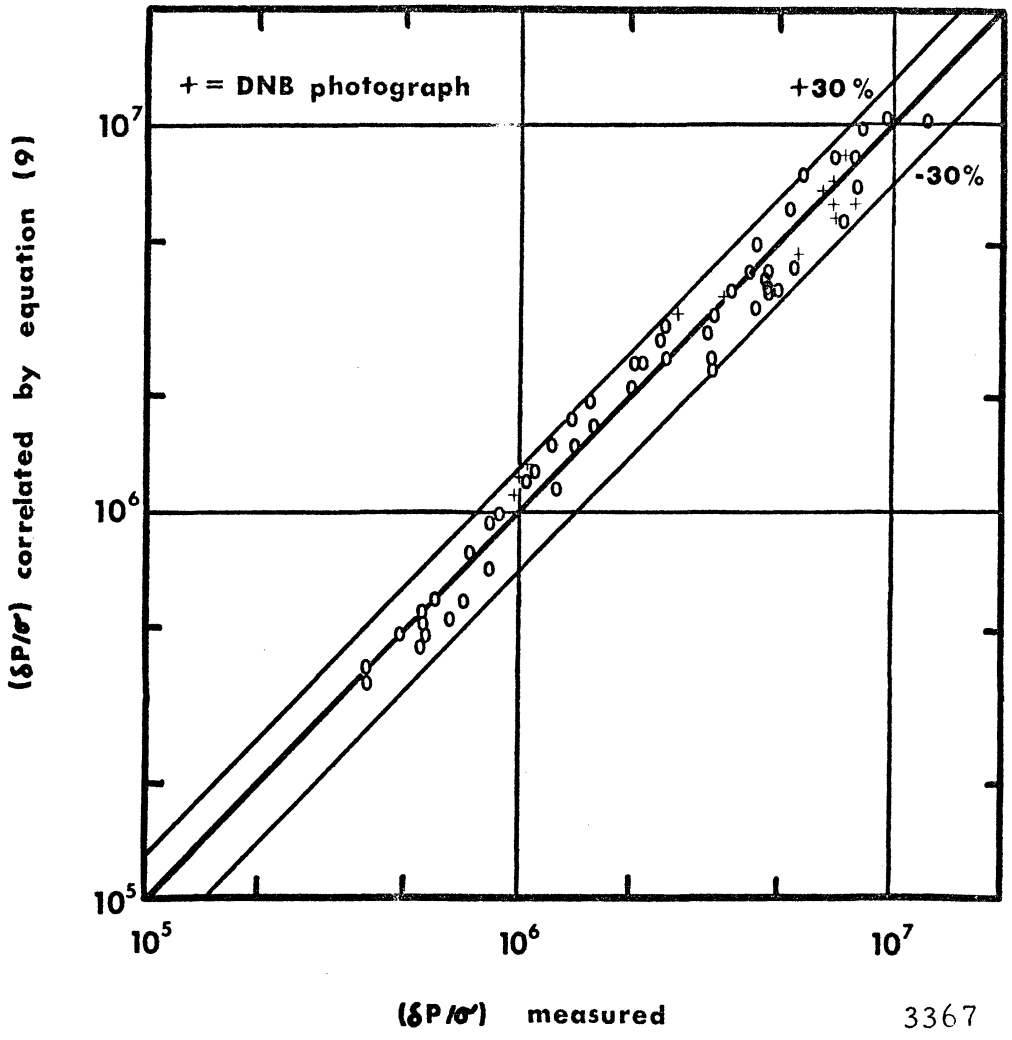

Figure 22. Nondimensional correlation of bubble boundary layer thickness.

The coefficient of multiple correlation for equation (9) was 0.987. Thermal and transport properties in equation (9) were evaluated at the saturation temperature. Dimensional analysis was used to select the Prandtl, Weber, and Stanton numbers as the correlating parameters. A total of 16 different nondimensional groups were systematically applied to this data, as in the derivation of equation (3). The parameter combinations of equations (8) and (9) provided the best fits to the measured values in terms of standard errors of estimate, coefficients of multiple correlation, and standard errors of the regression coefficients.

Jiji and Clark[36] photographically measured and correlated the bubble boundary layer thickness over the entire length of a heater strip in subcooled boiling of water at pressures up to 1000 psia. Their correlating equations were

$$\delta = 6 \times 10^{-4}(\Delta T_{sc})^{-1.163}(G)^{-0.504}(q")^{1.256}(\Delta X_i)^{0.534} \qquad (10)$$

and

$$\frac{\delta p}{\sigma} = 8.54 \times 10^{4}(St)^{0.443}(Pr)^{-1.742}\left[\frac{\rho_l}{\rho_v} - 1\right]^{-0.6} \times \left[\frac{q"\Delta X_i}{\mu h_{fg}}\right]^{-0.302}\left[\frac{p\Delta X_i}{\sigma}\right]^{0.237} \qquad (11)$$

where ΔX_i was the distance between the boiling inception point X_i and the point X at which the bubble boundary layer thickness was measured.

A comparison of equations (8) and (9) with equations (10) and (11) shows a general agreement on the influence of the significant parameters. That is, the thickness of the bubble boundary layer increases as the heat flux and distance down the heater increase and decreases as the pressure, subcooling, and mass flow rate are increased. However, there is some disagreement between the character of the bubbly flow in Jiji and Clark's work and the flow observed in this research. Quoting from reference 36, "The increase in [bubble boundary layer] thickness is primarily the result of an increase in bubble size. Furthermore, since the bubble boundary layer thickness at a given location along the strip is determined by the size of an individual bubble at that location, it follows that correlation equation (10) or (11) could be used to predict bubble size." Figures 6 to 13 show that the bubble sizes were much smaller than the bubble boundary layer thickness in high pressure Freon-113. Thus the sizes of the largest bubbles correlated in Figure 15 were nearly an order of magnitude smaller than the sizes of the bubble boundary layers correlated in Figure 21. Jiji and Clark studied mass

velocity and subcooling ranges comparable to the present work although they limited heat flux to less than 50 percent of CHF. Both their study and this research were in the so-called "bubbly" flow regime.

The apparent contradiction in these observations can be resolved on the basis of the two regimes which exist in bubbly flow as it is encountered in subcooled nucleate boiling. The regime is determined by the pressure and the heat flux. The pressure influences the size of the bubbles. Recalling the discussion in the Bubble Size and Distribution section above, for example, it was noted that pressure was the determining factor between the subcooled DNB theory of Fiori and Bergles and the theory of Dean. That is, low pressure DNB was attributed to the deterioration of bubbly flow by the formation of vapor slugs while high pressure DNB was attributed to bubble boundary separation.

The heat flux determines whether the bubbles will be attached to or detached from the heated surface, and the heat flux at which detached bubbles begin to occur has been called the point of net vapor generation.[25] All of Jiji and Clark's photographs, being limited to less than 50 percent of CHF, were apparently taken at heat fluxes below the point of net vapor generation while all of the photographs in this research were taken at heat fluxes beyond that point. Lippert[37] has photographed the high pressure

bubbly flow regime in the subcooled boiling of Freon-113. In his study of the point of net vapor generation there were photographs at high heat flux which showed a bubble boundary layer composed of many bubbles, all smaller than the boundary layer thickness. His research also contained photographs at low heat flux which showed boundary layers that were only one bubble diameter thick.

It is concluded that in subcooled flow boiling there are two regimes of bubbly flow. At low pressure and low heat flux the bubbles are large and confined to the region of the heated surface. The bubble boundary layer thickness is approximately equal to the size of the largest bubbles. As the heat flux approaches CHF the bubbles coalesce to form large vapor slugs. At high pressure and high heat flux the bubbles are small and migrate away from the wall so the bubble boundary layer thickness is much larger than the size of the largest bubbles. The dividing line between the two types of bubbly flow is about 800 to 1000 psia in water (100 to 140 psia in Freon-113).

Observations of the DNB Mechanism

The boiling crisis in this research was characterized by an abrupt increase in the heater temperature. Any theory which predicts DNB under these conditions of high

pressure, high subcooling and high mass flow rate must account for the abrupt decrease in the heat transfer coefficient. This was the intuitive appeal to the boundary layer separation model discussed in Chapter 1. That is, an abrupt change in the flow pattern at DNB would explain the abrupt change in the heat transfer mechanism.

This research was designed to provide photographic recordings of any abrupt changes in two-phase flow pattern at DNB. On the basis of the high quality photographs obtained in this research, it is concluded that no such changes occur. In previous sections of this report it has been shown that there are smooth transitions in the size, character, and motion of the bubbles and the bubble boundary layer as the heat flux is increased to the CHF. The results have shown that the character of the bubbly flow regime in high pressure subcooled boiling is somewhat different than was assumed in previous theoretical models; i.e., the bubbles are much smaller than the bubble boundary layer. The fact remains, however, that there is no abrupt change in the character of the flow at DNB.

If boundary layer separation were the causal mechanism for DNB then the photographs should have shown abrupt changes in (1) bubble flow trajectories above the DNB location, (2) slope of the bubble boundary layer just

upstream of the DNB location, and (3) velocity and trajectory of the vapor on the heater. None of these changes were observed.

There are two basic approaches to conceptualizing the subcooled boiling crisis--a heat transfer approach and a momentum transfer approach. Each approach has support from this research. For example, Figures 17-19 showed that the bubble size distribution and population density near the heater changed with increasing heat flux to provide an increasingly effective barrier between the heater and the subcooled liquid. This suggests a model based upon a thermal boundary layer or a heat transfer concept of DNB. On the other hand, Figure 20 showed that while the vapor velocity in regions away from the heater exceeded the liquid velocity, the liquid velocity gradient exceeded the vapor velocity gradient near the heater at DNB. This suggests a model based on a two-phase momentum boundary layer or a momentum transfer concept of DNB. This duality of concepts was first suggested by Tong.[12] On the basis of the results of the present research it is recommended that future efforts in theoretical modeling of subcooled DNB include consideration of both the thermal and the momentum boundary layers.

One final observation was made regarding the character of the flow pattern at DNB. This observation is admittedly

intuitive and it is based upon somewhat subjective interpretation of the area of poorest resolution in the photographs. With these words of caution, consider Figures 12 and 13.* The photographs in Figure 13 were taken just after DNB. There was a thin, intermittent vapor layer which extended from the downstream end of the heater to just upstream of the DNB-detecting thermocouple. The vapor layer was approximately 0.010 to 0.015 inch thick. No such vapor layer is seen in the pre-DNB photographs of Figure 12, although the bubbles on the heater are large and cover most of the surface area. Figure 11 was taken at DNB; it also shows an intermittent vapor layer approximately 0.010 inch thick on the heater surface. Similar observations were made on other post-DNB photographs. From these observations it is concluded that DNB occurred for the conditions of this research because of vapor flow stagnation in a very thin layer on the heater. Recall the following: (1) Figure 20 showed that the vapor velocity was low on the heater at DNB, (2) Figures 17-19 showed that the bubble size on the heater was largest at DNB, and (3) the bubbles moved along the heater before departure since the axial liquid velocity was much higher than the bubble rise velocity or the turbulent mixing velocity. Thus as DNB was approached, the bubbles on the heater began to pile up on one another towards the downstream end of the heater. The phenomenon

---

*More detail was available in the original prints.

just described is analogous to a traffic jam on an expressway; i.e., the momentary slowing of a few automobiles can cause a dense traffic flow to quickly slow down and back up for long distances.

The bubbles that slowed or momentarily stagnated on the heater were not large enough to cause separation of the bubble boundary layer. Their thickness of about 0.010 inch was sufficient, however, to thermally insulate the heater. A simple one-dimensional heat conduction calculation showed that a vapor layer 0.010 inch thick was sufficient to reduce the boiling heat transfer coefficient by two orders of magnitude. It is recommended that future efforts to theoretically model the boiling crisis should consider as a possible causal mechanism the sudden stagnation of the small bubbles on the heated surface.

Chapter 6

CONCLUSIONS

The following conclusions are restricted to the parameter ranges investigated.

The two-phase flow regime in high pressure subcooled boiling is bubbly in which small vapor bubbles form a flowing boundary layer along the heated surface. At high heat flux the thickness of the bubble boundary layer is much larger than the diameters of the largest bubbles.

Bubbles move along the heated surface at velocities which increase with size. The bubble size and size distribution on the heater increase as heat flux is increased and decrease as mass velocity is increased.

Bubbles coalesce on and above the heater. The largest bubbles occur at locations away from the heater and are the result of coalescence after departure from the heater.

The mechanism by which the wall void fraction increases with heat flux is first by simultaneous increases in bubble size and population density at low heat flux and then by increase in size and decrease in population density because of coalescence at high heat flux.

At DNB the local slip ratio between vapor and liquid velocities is greater than 1 except in a very thin region on the heated surface. The volume average slip ratio is apparently greater than 1 at DNB.

At DNB there are no abrupt changes in bubble size, bubble population density, bubble flow trajectory, bubble boundary layer thickness, or bubble boundary layer slope. That is, there is no abrupt change in flow regime at DNB.

A thin intermittent vapor layer forms on the heated surface at DNB. The thickness of the layer is approximately equal to the bubble departure size. It is thinner, however, than the diameters of the largest bubbles in the bubble boundary layer, and it is thinner than the bubble boundary layer by approximately a factor of ten.

Appendix A

FLUID-TO-FLUID MODELING OF THE FLOW-BOILING CRISIS

The purpose of this appendix is to sketch the approaches taken by others to determine fluid-to-fluid modeling criteria for two-phase flows, including the boiling crisis. The discussion shows that the experiment apparatus and conditions used in this research adequately simulate boiling crisis conditions in a high pressure water system.

Modeling of the flow-boiling crisis requires geometric and dynamic similarity. Dimensional analysis is the classical method of achieving dynamic similarity between geometrically similar systems. The approach used for problems whose governing equations are not well known consists of listing all parameters known to control the phenomenon, forming dimensionless groups of these parameters, and assuring that the modeling and modeled systems assume the same value for each dimensionless group. The number of dimensionless groups can be found by the Buckingham π theorem. Construction of two-phase flow scaling laws has not been accomplished by this method because of the large number of governing parameters and the lack of knowledge concerning their relative importance. Thus it has been impossible to obtain complete equality between model and prototype for all the dimensionless groups.[19]

Before describing alternative modeling techniques, first consider the similitude requirements. Geometric similarity means similar channel shape, size and length. However, for bubble size much smaller than channel size, such as bubbles in subcooled flow boiling with an equivalent water pressure of 2000 psi, the effects of channel shape and size on DNB are negligible, except as the size affects the Reynolds number.[14,17,24] Furthermore, under the "local conditions concept"[21,25] the same hydrodynamic and thermodynamic conditions should be present at the boiling crisis regardless of the heated length to that point. Consequently, the two-dimensional short test section used in this research did not affect the general applicability of the observations.

Dynamic similarity requires both hydrodynamic and thermodynamic similarity because heat, phase, and momentum exchange are involved in flow boiling. Hydrodynamic similarity means similar flow patterns and similar velocity and shear distributions. Similar velocity and shear distributions require equal Reynolds numbers. Similar flow patterns require equal Froude numbers, equal volumetric flow concentrations $Q_v/(Q_l + Q_v)$, and equal liquid-to-vapor density ratios ρ_l/ρ_v.[17] When the Froude number is large, as it was in this research, then inertia forces are much

greater than gravitational or buoyant forces. Therefore, the test section can be either horizontal or vertical without influencing the results.

Thermodynamic similarity implies a similar heat transfer mechanism and equivalent thermodynamic properties of model and prototype fluids. Thermodynamic properties are usually related by reduced pressure. However, water is an abnormal fluid in this respect and the density ratio ρ_l/ρ_v has been shown to be more significant than the reduced pressure for pressure scaling.[16,19] Figure A.1 shows the density ratio versus pressure relations for water and Freon-113. Equivalent pressure conditions in Freon-113 and water can be read from constant ρ_l/ρ_v lines in this figure.

Several approaches have been taken to develop scaling laws for the flow-boiling crisis. Barnett (see reference 19) systematically excluded some parameters known to influence the boiling crisis and then used dimensional analysis to derive scaling laws. This approach has not received strong support because the parameters that had to be eliminated have too strong an influence.[17,19,20] Staniforth and Stevens (see references 17 and 20) empirically determined CHF scaling factors between Freon-12 at 155 psia and water at 1000 psia for fixed values of L/D, ρ_l/ρ_v,

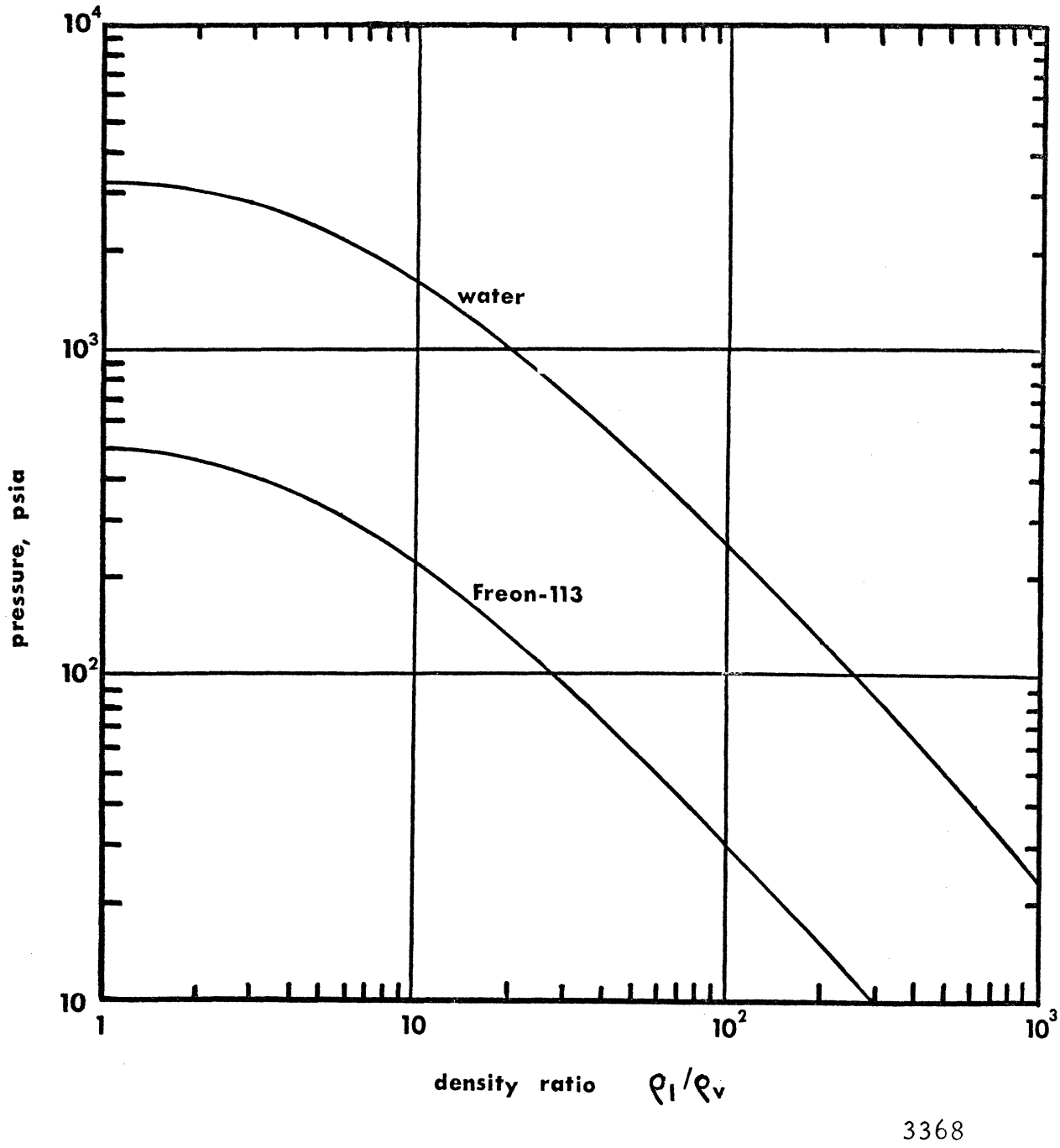

Figure A.1. Density ratio versus pressure for water and Freon-113.

and inlet subcooling. Another more general scaling approach was suggested by Stevens and Kirby (see references 17, 19, 20, 22) for saturated flow boiling. The method was improved by Staub,[21] and extended by Tong, et al.,[17] to the subcooled boiling regime. It is a graphical technique requiring the matching of two empirical CHF correlations with an empirical scaling factor which needs to be found but once for any combination of model and prototype fluids.

Tong, et al.,[17] also developed a boiling crisis scaling law based on thermodynamic similarity as expressed by the "boiling number (Bo)" and hydrodynamic similarity as expressed by a two-phase-flow friction factor. The CHF scaling factor was found to be a function of reduced pressure of the model fluid and the critical specific volume ratio and subcoolings of model and prototype fluids. Other scaling approaches[20,22] which are entirely empirical are useful only for the conditions and fluids tested and perhaps for a specific checking of some eventual "universal scaling law" for fluid-to-fluid modeling of two-phase phenomena.

Table A.1 summarizes the results of these recent efforts in this research area. It has been shown[23] both qualitatively and quantitatively that the same mechanism causes the boiling crisis in saturated boiling of Freon and

water. The techniques applied by Tong, et al.,[17] quantitatively establish this similarity for the subcooled boiling crisis. On this basis Freon-113 can be used, as was done in this research, to photographically study the qualitative character of the subcooled boiling crisis and the results can be extended to water.

Reference	Crowley[16]	Boure[19]	Dix[20]	Tong[17]	Groeneveld[22]	Stevens[23]
Derivation of scaling law	Characteristic eqn. derived from continuity, momentum, energy	Empirical correction and dimensional analysis	Direct empirical technique	Physical model of bubble boundary layer	Optimization empirical technique	Empirical graphical technique
Phenomenon modeled	Hydrodynamic stability	Saturated boiling crisis	Saturated boiling crisis	Subcooled boiling crisis	Saturated boiling crisis	Saturated boiling crisis
Fluids considered	Water/Freon-113	Water/Freon-12	Water/ Freon-114	Water/Freon-113	Water/Freon-12	Water/Freon-12
Scaling Factors: L/D	1	1	—	independent	1	1
p	5.7 @ 2000 psi water	6.0 @ 2000 psi water	Not Given	5.7 @ 2000 psi water	6.45 @ 1000 psi water	6.54 @ 1000 psi water
G	—	1	$f(G, \frac{\rho_l}{\rho_v}, \frac{L}{D})$	—	1.42	1.40
q"	6	12.8	Not Given	20 $f(P_{r,F}, \frac{v_{c,F}}{v_{c,W}}, \Delta T_{sc})$	17.8	16.8
ρ_l/ρ_v	1	1	1	1	1	1
$\Delta h_i/h_{fg}$	1.12	1.10	1	—	1	1
Fr	1	1.70	—	—	—	—
Re	1	—	—	1	—	—
Bo	—	1	1	1	—	1
Other scaling factors	V_l:1	—	—	—	X:1	D:1

Table A.1. Fluid-to-fluid scaling factors for two-phase flow phenomena; scaling factor F≡ prototype parameter/model parameter.

Appendix B

EQUIPMENT AND INSTRUMENTATION

Centrifugal Pump

The pump was a Berkeley model 1-1/2 WSR built by the Berkeley Pump Company and designed primarily for liquid metal service. All wetted parts were constructed of 300 series stainless steels. It was a belt-driven, overhung, centrifugal sump type pump rated for 40 gpm at 45 feet of head. Its shaft seal was rebuilt to permit pump inlet pressures up to 400 psi rather than atmospheric pressure. This required building a new stuffing box to house a Borg-Warner type U-2625-5H7A hydraulically balanced, water cooled, mechanical seal constructed with stellite and carbon seal faces, teflon* gasketing, and 316 stainless steel. By careful press and lathe operations pump shaft run-out was reduced adequately for this more sophisticated seal. The two shaft bearing assemblies were replaced.

Pump Drive

The pump was driven by four V-belts in parallel from a variable speed fluid coupling. The coupling was driven

---

*DuPont trademark

by a 20 hp, 1760 rpm Delco induction motor. The fluid coupling allowed continuous adjustment of pump speed between 250 and 1800 rpm.

Throttle Valves

The two stainless-steel throttle valves were Powell 300-pound, bellows-sealed "Y" valves. There was slight uncorrectable stem packing leakage at high pressure because the stainless steel bellows had been broken.

Pipe, Flanges, and Fittings

Pipe and flange materials were 304 and 316 stainless steel. All pipe was schedule 40, all flanges were 300 pound ASA with raised and grooved faces. The main loop was 1-1/2 inch pipe, the auxilliary loop was 1/2 inch pipe and 1/2 inch tubing. All instrument lines were 1/4 inch 304 stainless steel tubing. All tube fittings were 304 stainless steel "Swagelok" by Crawford Fitting Company.

Gaskets

All pipe flanges were sealed with Johns-Manville Style 913 "Spirotallic" gaskets. The seal area consisted of alternate windings of 304 stainless steel and white Canadian asbestos. Gaskets for the test section windows and heater pedestal were neoprene bonded asbestos, Johns-Manville material type 76.

Pressurizer

The loop was pressurized with compressed dry air supplied from a regulated bottle. The air tank was separated from the main loop by about ten feet of 1/4 inch stainless steel tubing.

Freon Filter-Dryer

The "catch-all" filter-dryer was a model C-484-P supplied by Sporlan Valve Company. It performed the following functions: water removal by absorption on desiccant; particle removal by trapping in porous desiccant; acid removal (from oil or Freon decomposition) by adsorption on desiccant. The desiccant was a blend of charcoal and activated alumina in the form of a sintered core which was periodically replaced a total of 3 times during the three months of data collection.

A.C. Loop Heaters

Main loop piping except the test section was encased in "clam shell" type resistance heaters supplied by the Hynes Electric Heating Company. The heaters were surrounded by a three-inch thick annulus of asbestos contained in sheet steel covers. The 220 volt, 3-phase heaters provided 6.5 kw of power. Heating was automatically controlled to provide a preset loop temperature by two pairs of Partlow model BSR indicating temperature controllers and Allen-Bradley contactors.

D.C. Power Supply

The ribbon heater was powered by a Sorensen Model DCR60-40 silicon controlled rectifier. This 2400 watt unit delivered up to 40 amps at 60 volts. It was operated in a current limiting mode with voltage increasing according to the load (ribbon heater) resistance and Ohms law.

Flow Meter

Flow through the main loop was measured with an orifice plate. Pressures were sensed at upstream and downstream flange taps, transmitted across stainless steel sensing diaphragms, then through NaK filled capillary tubes to a Taylor "Transaire" volumetric differential pressure transmitter. This instrument incorporated a force balance pneumatic system which produced an air pressure output proportional to the applied differential pressure. The NaK filled tubes isolated the measuring element from the high temperature Freon loop. The flow meter system including upstream and downstream piping was calibrated with water using a weigh tank.

Pressure Gages

The principal pressure instrument was a Heise bourdon tube gage with a 10 inch diameter dial. It was manifolded to 10 pressure taps located throughout the facility. The bourdon tube was stainless steel; the gage range was 0-400 psi with 0.5 psi subdivisions. Test section inlet and outlet

pressures were also monitored by two Taylor bourdon tube pressure gages with high temperature, mercury filled sensing heads. These gages were 0-400 psi range with 5 psi subdivisions. Output of the Taylor ΔP transmitter was measured with a Helicoid gage with a range 0-30 psi and 0.2 psi subdivisions.

Pressure of air supplied by the building compressor was indicated by a 0-100 psi U.S. Gauge bourdon tube gage. Compressed dry air was regulated by a Hoke intermediate air pressure regulator.

All pressure instruments were calibrated with a dead weight tester just before installation in the new boiling heat transfer facility.

Coolant Thermocouples

Freon-113 temperature was measured by two 24-gage iron-constantan thermocouples. One was located 5.75 inches upstream of the ribbon heater at the center of the channel, the other was 5.75 inches downstream of the ribbon heater at the center of the channel. The former was a grounded junction type for ease of assembly into the flow development section, the latter was a bare junction type. Both were supplied by Omega Engineering with stainless steel sheathing, MgO insulation, and stainless steel compression fitting.

Heater Thermocouple

Temperature of the ribbon heater was measured by a grounded 38-gage iron-constantan thermocouple cemented in place behind the ribbon with Epoxylite-813, a 500°F epoxy. Stainless steel sheathed, MgO insulated wire was supplied by Omega Engineering. The hot junction was formed with a Dynatec inert atmosphere thermocouple welder. The thermocouple was placed in good mechanical contact with the ribbon heater and held there while the ribbon was cemented to its backing insulator. Contact was maintained between heater and thermocouple by the heater tensioning action of the pedestal during oven drying of the epoxy.

Appendix C

DATA

Table C.1. Critical heat flux data.

P, psia	ΔT_{sc}, °F	G, 10^6 lb/hr-ft^2	q''_{crit}, 10^5 Btu/hr-ft^2
148	50	1.97	1.97
149	51	1.97	1.97
152	52	3.01	2.26
152	52	3.01	2.32
154	64	2.07	2.51
159	50	2.16	2.20
159	50	2.16	2.32
186	57	1.80	2.22
186	58	1.80	2.21
186	58	1.80	2.09
186	58	1.80	2.31
186	58	1.80	2.04
197	77	2.40	2.41
197	77	2.40	2.56
198	74	2.29	2.25
199	74	2.29	2.26
201	74	2.29	2.13
202	74	2.29	2.29
205	73	2.40	2.89
207	75	2.40	3.06
211	64	1.24	1.78
215	88	2.33	2.92
228	85	2.24	2.22
234	74	1.20	1.90
239	76	1.16	1.68
251	84	2.22	2.57
252	101	2.96	2.80
252	104	1.97	2.37
252	105	3.01	3.01
253	112	1.90	2.40
254	101	1.90	2.46
287	111	2.28	2.48
287	111	2.33	2.48
287	111	2.35	2.50
308	105	2.02	2.13
310	106	2.32	2.50
311	106	2.27	2.75
325	110	3.19	2.82
334	110	2.80	2.88

Table C.2. Data concerning the photographs

(M denotes Dynafax motion pictures,

* denotes DNB photograph.)

Negative Number	P psia	ΔT_{sc} °F	G 10^6 lb/hr-ft^2	q" 10^5 Btu/hr-ft^2	D_b inch	δ inch
8-1	105	39	1.23	0.271	0.0212	0.161
2	105	39	1.23	0.404	0.0272	0.230
4	105	39	1.23	0.479	0.0314	0.233
7	105	39	1.23	0.560	0.0323	0.234
11	105	39	1.23	0.649	0.0440	0.232
13	105	39	1.23	0.799	0.0483	0.254
16-0	284	112	2.35	0.720	0.0064	0.119
1	284	112	2.36	1.48	0.0135	0.158
2	284	112	2.36	1.83	0.0143	0.168
6	285	113	2.35	2.16	0.0150	0.192
10	285	112	2.35	1.72	0.0140	0.116
11	285	112	2.33	1.72	0.0142	0.178
12	286	111	2.35	2.20	0.0167	0.164
15*	287	111	2.35	2.50	0.0210	0.199
18*	309	119	2.28	2.49	0.0194	0.189
18-2	149	51	1.97	0.29	0.0089	0.109
3	151	52	1.97	0.63	0.0173	0.182
6	152	53	1.97	1.12	0.0255	0.178
8	149	51	1.97	1.77	0.0467	0.230
9*	148	50	1.97	1.97	0.0533	0.229
11	151	52	3.01	0.284	0.0056	0.086
12	151	52	3.01	0.628	0.0112	0.153
13	151	52	3.01	1.11	0.0163	0.162
15	152	52	3.01	1.72	0.0199	0.188
16*	152	52	3.01	2.26	0.0332	0.210
18	151	51	3.92	0.645	0.0099	0.145
19-1	251	106	1.97	0.570	0.0045	0.078
2	251	106	1.97	1.10	0.0090	0.115
3	251	106	1.97	1.69	0.0145	0.138
4	251	106	1.97	2.09	0.0189	0.192
6	251	106	3.01	0.623	0.0030	0.070
7	251	106	3.01	1.10	0.0054	0.089
8	251	106	3.01	1.69	0.0083	0.122

Table C.2., continued.

Negative Number	P psia	ΔT_{sc} °F	G 10^6lb/hr-ft^2	q" 10^5Btu/hr-ft^2	D_b inch	δ inch
19-9	252	106	3.01	2.11	0.0107	0.136
10*	252	105	3.01	3.01	0.0167	0.150
11	250	105	4.10	0.613	0.0023	0.065
13	251	105	4.10	1.10	0.0045	0.091
14	252	105	4.10	1.72	0.0080	0.110
15	253	106	4.10	2.42	0.0116	0.138
21-0	252	75	1.90	0.280	0.0052	0.080
3	253	76	1.90	1.66	0.0338	0.206
4	251	75	3.03	0.274	0.0026	0.071
6	252	75	3.03	1.10	0.0127	0.184
7	253	76	3.03	1.65	0.0187	0.177
12	351	114	1.96	0.60	0.0060	0.090
14	351	114	1.96	1.11	0.0101	0.119
17	352	114	1.96	1.63	0.0176	0.208
20	352	114	1.96	1.63	0.0172	0.164
22-3	350	113	2.96	0.607	0.0047	0.076
6	351	114	2.96	1.06	0.0075	0.098
10	351	114	2.96	1.73	0.0106	0.135
14	352	114	2.90	2.12	0.0128	0.142
17	350	113	4.02	0.605	0.0027	0.072
18	350	113	4.02	0.605	0.0030	0.078
20	350	113	4.02	1.07	0.0043	0.127
21	351	114	4.02	1.67	0.0075	0.139
M7*	154	64	2.07	2.51	0.0520	0.223
M8*	253	112	1.90	2.40	0.0233	0.204
M9*	308	105	2.02	2.20	0.0250	0.213
M10*	310	106	2.32	2.50	0.0281	0.178
M11*	311	106	2.27	2.75	0.0255	0.169
M12*	334	111	2.80	2.88	0.0229	0.156
M13*	325	110	3.19	2.82	0.0212	0.156

Appendix D

ESTIMATION OF ERRORS

The uncertainty in each measured parameter is presented below at a 95 percent confidence level. These uncertainties are combined statistically to evaluate the possible errors in calculated parameters. The relation used for determining uncertainties of calculated parameters was

$$W_r^2 = \left(\frac{\partial R}{\partial V_1} W_1\right)^2 + \left(\frac{\partial R}{\partial V_2} W_2\right)^2 + \ldots\ldots + \left(\frac{\partial R}{\partial V_n} W_n\right)^2 \qquad (D.1)$$

That is, if R is a linear function of n independent variables V_1, V_2 --- V_n, then the uncertainty interval W_r of the result was related to the uncertainty intervals W_1, W_2 --- W_n according to equation (D.1).

Measured Parameters

System pressure was measured at the exit end of the test section with a gage calibrated to ± 0.5 psi over the range 0-400 psi. The gage was read within ± 0.5 psi, the size of its subdivisions. Uncertainty in atmospheric pressure was less than ± 0.5 psi. The estimated total error in pressure due to these three independent sources of error was ± 0.4 percent at 250 psia.

System volumetric flow rate was measured by an orifice plate which was calibrated to within ± 0.8 percent for flows greater than three gpm. The error associated with transmitting the orifice pressure drop was ± 0.7 percent. The error in reading the flow pressure gage was ± 0.05 psi which was equivalent to a ± 1.4 percent error for the worst case of minimum flow rate. The estimated total error in volumetric flow rate due to these three independent sources of error was ± 1.8 percent at the minimum flow rate.

Errors associated with reading oscillograph records were estimated to be ± 0.015 inch. This corresponded to the following uncertainties: current, ± 0.08 amp; voltage, ± 0.03 volts; coolant thermocouples, ± 0.8°F, ribbon heater thermocouple, ± 1.8°F. For typical values of these recorded parameters, the errors were ± 0.4 percent of current, ± 0.3 percent of voltage, ± 0.3 percent of coolant temperature, ± 0.6 percent of ribbon temperature.

Galvonometers which recorded thermocouple signals were calibrated over full scale deflection (about four inches) and were found to be linear within ± 1.0 percent. Current and voltage recording galvonometers were linear within ± 2.0 percent over full scale deflections of seven inches.

These nonlinearity errors are independent of the reading errors described in the preceding paragraph.

Ribbon heater current was proportional to the voltage drop across a precision shunt which was calibrated to an accuracy of ± 1.5 percent. A random error of ± 1.0 percent was attributed to current measurements. The estimated total error in current due to these sources combined with the oscillograph errors was ± 2.7 percent.

Ribbon heater voltage was recorded directly on the oscillograph. A random error of ± 1.0 percent was attributable to voltage measurements. The estimated total error in voltage due to this source and to the oscillograph errors was ± 2.3 percent.

Coolant temperatures were measured with thermocouples which met calibration standards of ± 2°F. This error combined with the oscillograph errors gave an estimated total error in coolant temperatures of ± 1.3 percent.

Ribbon heater temperature was measured by a thermocouple which was fabricated from wire that met calibration standards of ± 2°F. Consistency checks between the three thermocouples (two in the coolant and one on the ribbon heater) showed agreement within the specified ± 2°F for temperatures up to 250°F with no power to the ribbon. Conduction error associated with the thin wires of the heater

thermocouple was estimated by the method of Schneider[30] to be approximately -5°F. The error attributable to measuring ribbon temperature on the insulated back surface was estimated to be approximately +4°F on the basis of a steady, one-dimensional conduction analysis. Another error was attributable to thermal contact resistance at the ribbon-to-thermocouple interface. This error grew larger with prolonged use of any particular ribbon because of breakdown of the epoxy cement during successive DNB excursions. Estimates of total wall temperature errors were made from the estimated wall superheat in boiling and found to vary from ± 2 percent for a newly-installed heater and thermocouple, to -20 percent for a heater and thermocouple which had been through DNB ten times. Ribbon heater temperatures were not used in the data reduction for this research. This thermocouple was a consistently good detector and indicator of the occurrence of DNB. This was confirmed by the simultaneity of its excursion with the ribbon voltage excursion.

The errors associated with determining the scale of an enlarged photograph from the known height of the flow channel were estimated to be ± 2.2 percent for the still photographs and ± 2.3 percent for the Dynafax motion photographs. The error for the large scale still photograph

scale was higher than might be expected because of fuzzy definition of the top of the flow channel. There was a ± 5 percent error attributed to scaling Fastax photographs on the basis of measured ratios between field of view and frame size.

The estimated error of measuring the diameter of a 0.010 inch bubble with a 0.02 inch subdivision rule was ± 3.5 percent for still camera photographs with 15x enlarg ment and ± 11 percent for Dynafax photographs with 4.5x enlargement. The estimated total error in bubble diameter thus ranged from ± 4.1 percent to ± 11.2 percent for a 0.010 inch bubble.

The estimated error of measuring the bubble boundary layer thickness was ± 5 percent for still camera photographs with 15x enlargement and ± 6 percent for Dynafax photographs with 4.5x enlargement. These errors are estimated as nearly equal because the Dynafax photographs with their wider field of view gave better perspective for determining the top of the layer. A ± 5 percent random error was attributed to measurement of bubble boundary layer thickness from still photographs because of the lack of sequential pictures to confirm the selection of a time averaged thickness. These errors combined with scaling errors gave estimated total errors in boundary layer

thickness of ± 7.4 percent for the still photographs and ± 6.5 percent for the Dynafax photographs.

The error associated with the frame rate of Dynafax photographs was estimated to be ± 1.0 percent on the basis of a frame rate calibration with a digital counter.

A ± 5 percent error was attributed to measurements of the distance traveled by a bubble between Dynafax frames separated by 0.00032 sec. (the minimum time used in vapor velocity calculations) when using a 0.02 inch subdivision rule.

Calculated Parameters

Ribbon heat flux was calculated from heater current and voltage measurements. Errors in calculating the surface area of the ribbon were negligible due to small fabrication tolerances. Combining current and voltage errors according to equation (D.1) resulted in an estimated heat flux error of ± 3.7 percent. This estimate does not include heat loss from the back of the heater by conduction to the test section. The heat loss was estimated to be less than 2 percent on the basis of a one-dimensional calculation.

Subcooling at the exit of the test section was calculated from the exit pressure and the exit coolant

temperature. The pressure error of ± 0.4 percent corresponded to a ± 0.4 percent error in saturation temperature. Combining saturation and exit temperature errors according to equation (D.1) resulted in estimated subcooling errors ranging from ± 3.5°F for test conditions of 250 psia and 80°F subcooling, to ± 3.7°F for test conditions of 350 psia and 115°F subcooling.

Vapor velocity was calculated from the measured displacement of bubbles between sequential Dynafax motion pictures and the measured frame rate of the camera. Combining the displacement and frame rate errors according to equation (D.1) resulted in estimated vapor velocity errors between ± 5.2 percent for minimum frame separation to ± 2.0 percent for frame separations typical of most of the measurements.

Average liquid mass flow rate was calculated from the measured volumetric flow rate and the liquid density tabulated as a function of temperature. The coolant temperature error of ± 1.3 percent was equivalent to a liquid density error of ± 0.6 percent. Combining the density and volumetric flow rate errors according to equation (D.1) resulted in an estimated mass flow rate error of ± 2.0 percent.

REFERENCES

1. L. S. Tong, "Heat Transfer in Water-Cooled Nuclear Reactors," Nuclear Engineering and Design, 6: 1967.

2. F. E. Tippets, "Critical Heat Flux and Flow Pattern Characteristics of High Pressure Boiling Water," General Electric APED Report GEAP-3766: April, 1962.

3. S. G. Bankoff, "On the Mechanism of Subcooled Nucleate Boiling, Parts I and II," Chem Eng Prog Symp Ser, 57, (32), 156: 1961.

4. Y. P. Chang, "An Analysis of the Critical Conditions and Burnout in Boiling Heat Transfer," USAEC Report TID-14004: 1961.

5. R. J. Weatherhead, "Hydrodynamic Instability and the Critical Heat Flux Occurrence in Forced Convection Vertical Boiling Channels," USAEC Report TID-16539: 1962.

6. W. R. Gambill, "Generalized Prediction of Burnout Heat Flux for Flowing Subcooled, Wetting Liquids," Chem Eng Prog Symp Ser, 59, (41), 71: 1963.

7. L. S. Tong, H. B. Currin, P. S. Larsen, O. G. Smith, "Influence of Axially Non-Uniform Heat Flux on DNB," Chem Eng Prog Symp Ser, 62, (64), 35: 1966.

8. L. S. Tong, "Boundary Layer Analysis of the Flow Boiling Crisis," Int. J. Heat Mass Transfer, II, 1208-1211: 1968.

9. S. S. Kutateladze and A. I. Leontiev, "Some Applications of the Asymptotic Theory of the Turbulent Boundary Layer," Proc. Third International Heat Transfer Conference, III, 1, AIChE-ASME, Chicago: 1966.

10. R. A. Dean, "Effect of Vapor Injection on Critical Heat Flux in a Subcooled R-113 (Freon) Flow," Ph.D. Thesis, University of Pittsburgh: 1970.

11. G. B. Wallis, "Use of the Reynolds Flux Concept for Analysing One-Dimensional Two-Phase Flow: Parts I and II," Int. J. Heat Mass Transfer, 11, 445-473: 1968.

12. L. S. Tong, "Theoretical Analyses of Subcooled Boiling Crisis," Paper Delivered to the Nuclear Congress of Rome: 1971.

13. M. P. Fiori and A. E. Bergles, "Model of Critical Heat Flux in Subcooled Flow Boiling," Paper B6.3, Fourth International Heat Transfer Conference, Paris: 1970.

14. L. S. Tong, L. E. Efferding, A. A. Bishop, "A Photographic Study of Subcooled Boiling Flow and DNB of Freon-113 in a Vertical Channel," ASME Paper 66-WA/HT-39: 1966.

15. Y. Y. Hsu, R. J. Simoneau, F. F. Simon, R. W. Graham, "Photographic and Other Optical Techniques for Studying Two-Phase Flow," Two-Phase Flow Instrumentation, 11th National Heat Transfer Conference, Minneapolis: August 1969.

16. J. D. Crowley, A. E. Bergles, "Fluid-to-Fluid Modeling of the Hydrodynamic Stability of Flow in Boiling Channels," ASME Paper 70-HT-28: 1970.

17. L. S. Tong, F. E. Motley, J. O. Cermak, "Scaling Law of Flow-Boiling Crisis," Paper B6.12, Fourth International Heat Transfer Conference, Paris: 1970.

18. D. C. Groeneveld, "Similarity of Water and Freon Dryout Data for Uniformly Heated Tubes," ASME Paper 70-HT-27: 1970.

19. J. A. Boure, "A Method to Develop Similarity Laws for Two-Phase Flows," ASME Paper 70-HT-25: 1970.

20. G. E. Dix, "Freon Modeling of CHF in Round Tubes," ASME Paper 70-HT-26: 1970.

21. F. W. Staub, "Two-Phase Fluid Modeling-the Critical Heat Flux," Nuclear Science and Engineering, 35, 190-199: 1969.

22. D. C. Groeneveld, "Similarity of Water and Freon Dryout Data for Uniformly Heated Tubes," ASME Paper 70-HT-27: 1970.

23. G. F. Stevens, R. V. Macbeth, "The Use of Freon 12 to Model Forced Convection Burnout in Water: The Restriction on the Size of the Model," ASME Paper 70-HT-20: 1970.

24. L. F. Glushchenko, "Correlation of Experimental Data on Critical Heat Fluxes in Subcooled Boiling," Heat Transfer - Soviet Research: January 1970.

25. L. S. Tong, Boiling Heat Transfer and Two-Phase Flow, John Wiley and Sons, N. Y.: 1966.

26. R. W. Murphy, A. E. Bergles, "Subcooled Flow Boiling of Fluorocarbons," Report DSR 71903-72, Engineering Projects Laboratory, Massachusetts Institute of Technology: January 1971.

27. "Freon Compounds and Safety," DuPont Bulletin S-16: 1969.

28. W. G. Hyzer, Engineering and High-Speed Photography, The MacMillan Company, N.Y.: 1962.

29. C. L. Kling, "A High-Speed Photographic Study of Cavitating Bubble Collapse," Ph.D. Thesis, The University of Michigan, ORA Report 03371-2-T: 1970.

30. P. J. Schneider, Conduction Heat Transfer, Addison Wesley, Reading, Mass.: 1957.

31. M. A. Styrikovich, A. E. Nevstrueva, G. M. Dvorina, "On Hydrodynamic Character of Burnout in Subcooled Liquid Boiling in Channels," ASME Paper 69-HT-59: 1969.

32. G. C. Treshchov, "Experimental Investigation of the Mechanism of Heat Transfer with Surface Boiling of Water," Teploenergetika, Vol. 4, No. 5: 1957.

33. W. M. Rohsenow, H. Choi, Heat, Mass, and Momentum Transfer, Prentice-Hall, Englewood Cliffs, N. J.; 1961.

34. S. C. Rose, Jr., P. Griffith, "Flow Properties of Bubbly Mixtures," ASME Paper 65-HT-58: 1965.

35. N. Zuber, J. A. Findlay, "Average Volumetric Concentration in Two-Phase Flow Systems," ASME Journal of Heat Transfer: November 1965.

36. L. M. Jiji, J. A. Clark, "Bubble Boundary Layer and Temperature Profiles for Forced Convection Boiling in Channel Flow," ASME Journal of Heat Transfer: February 1964.

37. T. E. Lippert, "Experimental Determination of the Heat Transfer and Vapor Void Characteristics of R-113 in Subcooled Flow at Boiling Inception and at the Point of Net Vapor Concentration," Ph.D. Thesis, University of Pittsburgh: 1971.

38. K. Kristofferson, Kris Kristofferson: The Silver Tongued Devil and I, Chappell and Company, Inc., New York: 1971.